38. Monitoring of the Neutral Atmosphere

Gunnar Elgered, Jens Wickert

Global navigation satellite system (GNSS)-based atmosphere sounding techniques have become a widely recognized and operationally used remote sensing tool. A major milestone of this development was the beginning of the continuous use of GNSS data for improving regional and global forecasts in 2006. The principle behind these techniques is the utilization of atmospheric propagation effects on the GNSS signals on their way from the navigation satellites to receivers on the ground or aboard satellites. The atmosphere delays the time of arrival and introduces a curvature of the signal path. These effects can be accurately estimated and be used for the monitoring of the atmospheric variability. There are two different observation geometries. Therefore, we focus in the first part of this chapter on ground-based networks which are used to estimate the amount of water vapor above each receiver site. The second part deals with the use of radio occultation measurements from GNSS receivers aboard low Earth orbit satellites for global atmosphere sounding. We introduce and describe both techniques which provide observations suitable for the short-term weather forecasting and the long-term time series for climate research and monitoring.

This chapter deals with two distinctly different geometries: observations using ground-based global navigation satellite system (GNSS) networks and occultation observations from low Earth orbit (LEO) satellites. These are illustrated by the sketches in Fig. 38.1. In both geometries, the refractivity along the propagating path is determined by the atmospheric properties mainly in terms of pressure, temperature, and humidity.

The main application of the ground-based geometry is to infer the water vapor content above each receiver site on the ground. In principle, all the water vapor can be found within the troposphere, ranging from the ground up to 8–15 km. With a reasonable view of the sky, there will always be a sufficient number of satellites visible in order to have continuous time series of the estimated water vapor content.

The radio occultation (RO) geometry is more dynamic, since here both the transmitting GNSS satellites and the receiving LEO satellites are in continuous motion with respect to the atmosphere. When occultations occur, height profiles of the refractive index in both the troposphere and the stratosphere are retrieved.

Because of very different geometries, these two methods use different processing techniques and different algorithms in the data analyses. They also produce completely different data products. Therefore, we first

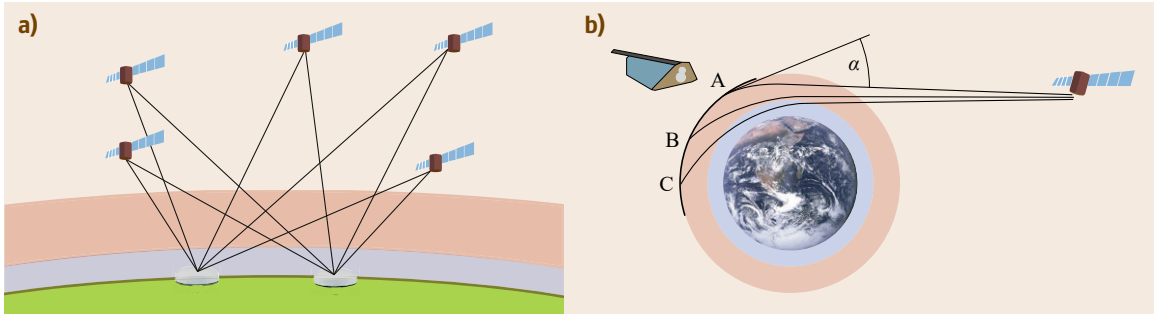

Fig. 38.1a,b Example geometries for ground-based observations (a) and ROs (b) of signals from GNSS satellites in a typical medium Earth orbit (MEO). The neutral atmosphere and the ionosphere are indicated by the *blue* and the *red* layers, respectively

discuss them separately. Applications of the remote sensing of the neutral atmosphere based on observations with ground-based networks are discussed in Sect. 38.1, while applications of GNSS receivers in LEO satellites are addressed in Sect. 38.2. The two geometries are of complementary nature, and their strengths for applications in forecasting and research related to atmospheric processes over different timescales, from turbulence phenomena to climate issues, are finally summarized in Sect. 38.3.

38.1 Ground-Based Monitoring of the Neutral Atmosphere

As described in Chap. 6, a GNSS signal from a satellite is delayed in the atmosphere compared to propagation in vacuum. The effect, often described as an excess propagation path, is estimated in the GNSS data processing. This means that using a receiver on the ground, it is possible to infer the integrated amount of water vapor (IWV) in the atmosphere.

Figure 38.2 summarize the possible use of GNSS data in three different types of applications. First, the GNSS data can be used as a standalone product, for example, for monitoring the IWV at a specific site over long time. Second, the GNSS data can be used to assess, or verify, the results from numerical weather models used in forecasting or climate research. Third, the GNSS data be combined with other data in order to increase the quality, for example, when assimilated into a numerical weather model in near-real-time weather forecasting.

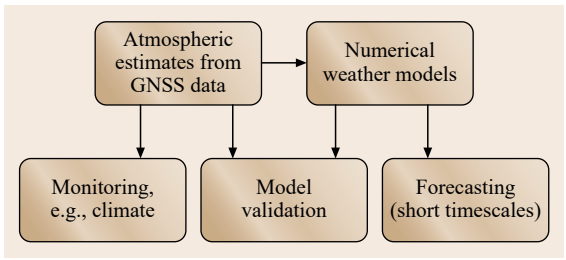

Fig. 38.2 Block diagram illustrating possible applications of atmospheric estimates from GNSS data in meteorology and atmospheric research

In some applications, it can be a strength to estimate and to work with an integrated quantity, but, of course, for many other applications, profile information is necessary. For the ground-based geometry, the advantage is the accurate estimates of the IWV. This section focuses on this application, although attempts to retrieve profile information using tomographic methods is also discussed.

The radio-based space geodetic techniques of very long baseline interferometry (VLBI) and GNSS are affected by the atmosphere in terms of variations in the refractivity in the atmosphere which delays the time of arrival, the fundamental observable. It was shown in [38.1] and [38.2] that the estimated propagation delays from global positioning system (GPS) data, together with ground pressure observations, resulted in time series of the delays induced by the atmospheric water vapor, and they were in agreement with independent ground-based measurements from microwave radiometry.

The necessary background material needed in order to describe the estimation of propagation delays affecting signals, penetrating the atmosphere on their way to a receiver on the ground, is presented in Chap. 6. Let us here just repeat the basic definitions. The elevation dependence of the propagation delays is modeled by mapping functions, one for the hydrostatic delay and

one for the wet delay in the geodetic GNSS data processing. The end result is the equivalent zenith total delay (ZTD). The ZTD

$$Z_t = Z_h + Z_w \tag{38.1}$$

is hence the sum of the zenith hydrostatic delay (ZHD)

$$Z_h = 10^{-6} \int_{h_0}^{h_\infty} N_h(z)\, dz \tag{38.2}$$

and the zenith wet delay (ZWD)

$$Z_w = 10^{-6} \int_{h_0}^{h_\infty} N_w(z)\, dz\,, \tag{38.3}$$

which are obtained from the integration of the hydrostatic (N_h) and wet (N_w) refractivities along the vertical propagation path from the height h_0 of the receiver to a point h_∞ outside the atmosphere.

With a sufficient number of observations in different directions during a defined time period, a refinement of just estimating an equivalent zenith propagation delay is possible. By defining linear horizontal gradients in the hydrostatic and wet refractivity profiles, an integrated parameter, normally referred to as the horizontal gradient, can be inferred. It was shown in [38.3] that by estimating horizontal gradients in the processing of GNSS data, the geodetic result improves significantly. It is today a common practice to estimate these gradients, although the use in meteorological applications has so far not been extensive. This potential will be further discussed later.

Another concept that occurs in the modeling of the neutral atmosphere is that of slant path delays. A simple method is to add the equivalent zenith delay and the estimated linear horizontal gradient and thereby model a specific delay in any given direction. The idea of adding, in addition, the residual delay toward each satellite from the GNSS data processing has also been proposed but shown to be wrong in the sense that systematic errors are introduced [38.4]. Instead, additional atmospheric parameters have to be estimated simultaneously, for example, by introducing tomographic methods.

38.1.1 Accuracy of Propagation Delays

Before describing the different applications of ground-based GNSS meteorology, we will review the error sources that determine the quality of the input data, that is, the estimated ZTD as described in Chap. 6. The uncertainty of these excess propagation delays depends on several effects. Here, we review the relative importance of the type of mapping function used, mismodeling of ionospheric effects (Chaps. 6 and 39), and effects caused by antennas and signal multipath.

Mapping Functions

The mapping functions define the elevation dependence of the hydrostatic and the wet delays, and are, therefore, an important parameter when estimating the atmospheric effect in the data processing. The development of more and more accurate mapping functions is described in Sect. 6.2.4. Many qualitative comparisons of mapping functions have been carried out over the years. Most mapping functions perform very well at high elevation angles, so when analyzing the accuracy of mapping functions, it is most interesting to focus on the results that are obtained at the lowest elevation angles, where the accuracy of the functions is decreasing. This means that, for each application, there is an optimum elevation cutoff angle. Low-elevation observations improve the geometry and reduce the formal error of the ZTD, but, at the same time, they introduce larger mapping function errors.

The *Niell* mapping function (NMF, [38.5]) has often been used due to its simplicity. It does not require any additional meteorological data; it only requires the location of the site and the time of the year. The size of uncertainties involved can be assessed by comparing the estimated ZTD using different mapping functions. As an example, a mean reduction of the ZTD of −2.6 mm was observed for 12 sites in Antarctica when changing from the NMF to the Vienna mapping function (VMF1) using elevation angles down to 7° [38.6].

Depending on the application, the need to include observations at low-elevation angles will vary. This is discussed later and now we just note that the choice of the mapping function is more or less irrelevant for GNSS meteorology if it is going to be used with observations acquired at elevation angles above say 15–20°.

Mismodeling of Ionospheric Effects

The accuracy of the ionospheric model used in the GNSS data processing affects the accuracy of the ZTD. Errors in the modeling of the signal delays caused by the ionosphere are more or less absorbed into the delays estimated for the neutral atmosphere, that is, the ZTD. To the authors' knowledge, no study has been directly focused on the accuracy of the estimated ZTD for different methods to correct for the ionospheric influence. However, there have been studies addressing the accuracy of the estimated position for different methods of handling the ionosphere. There is a strong correlation between the estimated vertical coordinate and

the estimated ZTD. A relative error in the ZTD is approximately three times smaller than the error in the estimated vertical position. The factor depends on the geometry, in terms of the elevation cutoff angle used for the observations [38.7]. Therefore, studies on the influence of the ionospheric model on the estimated site position indirectly provide information on the accuracy in the estimated ZTD.

The inclusion of higher order terms in the ionospheric model showed a systematic effect at the level of several millimeters in the station positions [38.8]. Later a more accurate model of the International Geomagnetic Reference Field (IGRF) was used [38.9]. Different models for the geomagnetic field have also been studied in [38.10], resulting in the recommendation that corrections for higher order ionospheric effects shall be included, particularly in equatorial regions and over periods of solar maximum when the ionosphere is more active. Given the 11-year-long solar cycle, it is reasonable to assume that the recommendations from such studies will depend on the timescale of the application.

Antenna Phase-Center Variations

Antenna phase-center variations exist both at the satellite antenna and at the receiving antenna on the ground. It has been shown that phase center variations (PCVs) (Chap. 17) have a significant influence on the estimated delay in the neutral atmosphere [38.11], and hence also on the IWV. The variation depends on the nadir angle from the satellite to the ground or, equivalently, the elevation angle of the satellite seen from the ground. The main effect is a bias-type of error but will, of course, change with changing geometries. Recommendations for modeling antenna PCVs exist (Chaps. 19 and 25) and shall be used in order to reduce their influence. Proper modeling of PCVs is especially relevant for climate-related applications investigating (small) long-term trends in the IWV. An assessment of the effect caused by the introduction of new GPS satellite types with different antenna phase patterns revealed an artificial trend of up to roughly $0.15\,\mathrm{kg/(m^2\,year)}$ for the estimated IWV over a five-year period [38.12].

Signal Multipath

Signal multipath (Chap. 15) degrades the precision of the arrival time of the signal from the satellite. The effect will have a more or less strong dependence on the elevation angle of the direct signal, depending on the local electromagnetic environment at the receiving antenna. It is difficult to model since the environment is changing. For example, the reflective properties of the ground change when it is covered by (rain) water, snow, and soil moisture, if soil is present. It has been shown that the effect of signal multipath can be reduced by mounting a plate with a microwave-absorption material just below the GNSS antenna [38.13].

38.1.2 From Delays to Water Vapor Content

The primary estimate from the data processing for the atmospheric influence is the ZTD. For some meteorological applications, the ZTD can be used directly, whereas other applications require the time series of the IWV, for example, when validating results from other instruments where the IWV is the primary output.

The overall data flow is illustrated in Fig. 38.3. The main operation is first to subtract the ZHD from the ZTD in order to obtain the ZWD. Thereafter the IWV is calculated from the ZWD. It shall be pointed out that the use of numerical weather models is not necessary. It is, however, common that information from such models is used to derive and optimize mapping functions,

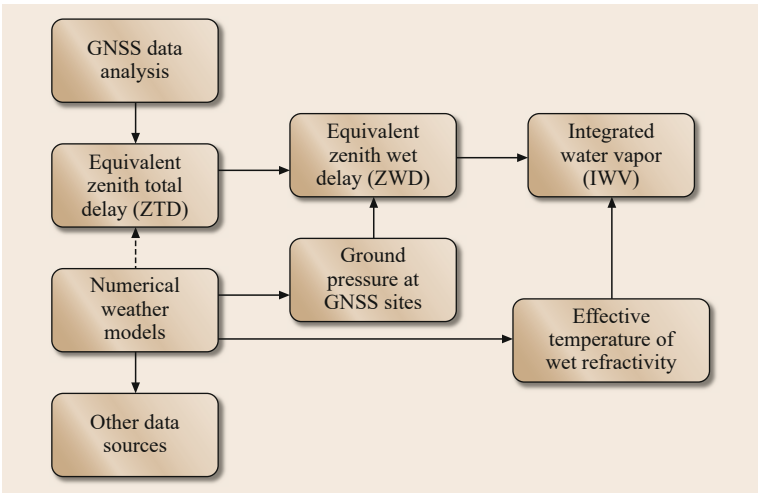

Fig. 38.3 The data flow for different applications in ground-based GNSS meteorology. Depending on the application the timescales of the data flow between the different operations can vary from seconds to years

and they may also provide a priori information about the atmosphere to the GNSS data analysis. Since the mapping functions for the hydrostatic and the wet delays are different such a priori information has been shown to increase the accuracy of the estimated ZTD [38.6]. As will be discussed below, there are also alternatives to numerical weather models for the estimation of the ground pressure and the effective temperature of the wet refractivity.

Before discussing these further, we note that both steps will require some knowledge of the state of the atmosphere, mainly the profiles of pressure and temperature. For applications such as weather forecasting, up-to-date knowledge already exists in the numerical weather models, and, in such cases, there is no need to compromise by using less accurate relations. Instead, the normal procedure is then to assimilate the ZTD directly into the numerical weather model.

From ZTD to ZWD

The first step is to subtract the ZHD from the ZTD. Hence, the uncertainty in the ZHD is directly transferred to the ZWD via (38.1) and (6.50). The only observable needed for the calculation of the ZHD is the ground pressure, assuming that the latitude and the height of the station are approximately known. This assumption is indisputable for ground-based GNSS networks used for meteorological applications. There are basically two possibilities to obtain the ground pressure: either to use a barometer at the site or to use the analysis from a numerical weather model which has input observations of the ground pressure of a sufficient accuracy from the surrounding area.

Commercially available pressure sensors provide accuracies much better than 0.5 hPa. Figure 38.4 depicts the observed differences between three barometers at the Onsala VLBI site. Comparison with a barometer from the Swedish Meteorological and Hydrological Institute (SMHI) shows that the present sensor has an absolute accuracy at the level of better than 0.2 hPa. Over the time period of interest, the SMHI barometer has been calibrated approximately every second year, and it is traceable to the SI unit within 0.1 hPa.

Several studies assessing the accuracy of deriving the ground pressure at the site from numerical weather models have been performed. The uncertainty of the ground pressure derived from the European Centre for Medium-Range Weather Forecasts (ECMWF) has been evaluated [38.16]. They compared the interpolated ground pressure from the ECMWF analysis to the local ground measurements at more than 60 globally distributed GPS sites using one year of data. The results revealed an agreement with an overall mean bias and a standard deviation of 0.0 hPa and 0.9 hPa, respectively. A similar test, using more than 10 years of data for the GPS site at the Onsala Space Observatory, resulted in a mean bias and a standard deviation of 0.1 hPa and 0.6 hPa, respectively [38.17]. Pressure sensors of the World Meteorological Organization (WMO) were compared to nearby (< 50 km) locally installed sensors and biases of less than 1 hPa for more than 90% of the stations were found [38.18]. Similar results were obtained in [38.19] using independent data sets and models.

These uncertainties together with other parameters in (6.50) are summarized in Table 38.1. Assuming uncorrelated errors, these four add up to a relative uncertainty equal to $2.2 \cdot 10^{-4}$. To this uncertainty shall also be added the uncertainty in the ground pressure. This is illustrated in Fig. 38.5, where the ground pressure uncertainties of 0.2 hPa and 1.0 hPa are assumed to be relevant for the observations and models, respectively. We conclude that the major contribution to the total ZHD uncertainty is from model uncertainties of 1.0 hPa, equivalent to a relative error of $1 \cdot 10^{-3}$, which corresponds to ≈ 2 mm in the ZHD. If actual high-quality pressure observations are used instead, the

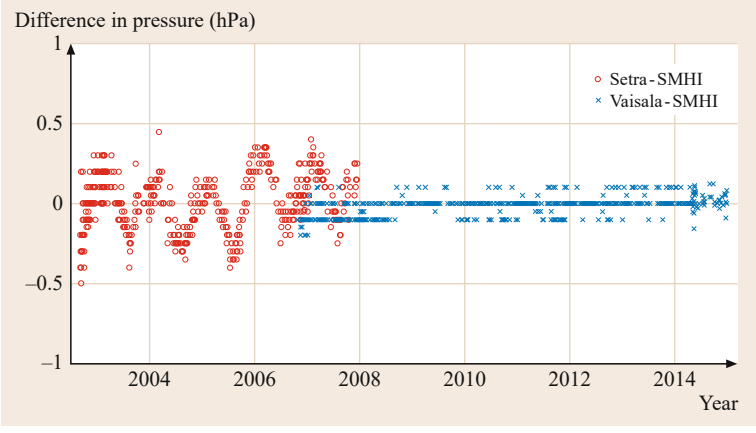

Fig. 38.4 Differences in the observed pressure by three different barometers. The Setra barometer was the standard unit at geodetic VLBI stations when the Mark III system was introduced. The small annual variations are likely caused by a sensor sensitivity to temperature. These are completely removed when the new barometer from Vaisala was connected to the VLBI system

Table 38.1 Parameters used to calculate the ZHD, their uncertainties, and the resulting uncertainties in the ZHD (Z_h)

Parameter	Value	Uncertainty	Unit	Relative uncertainty	Reference
k_1	77.6890	0.015	K/hPa	$1.9 \cdot 10^{-4}$	Table 6.2
R	8.3144621	0.0000075	J mol^{-1} K^{-1}	$9.0 \cdot 10^{-7}$	[38.14]
M_d	28.9644	0.0014	kg kmol^{-1}	$4.8 \cdot 10^{-5}$	[38.15]
g_{eff}	≈ 9.784	0.001	m s^{-2}	$1.0 \cdot 10^{-4}$	(6.51), [38.15]
p_0, case 1	≈ 1000	0.2	hPa	$0.2 \cdot 10^{-3}$	Typical observation, see the text
p_0, case 2	≈ 1000	1.0	hPa	$1.0 \cdot 10^{-3}$	Typical model, see the text
Z_h, case 1	≈ 2.28	$0.7 \cdot 10^{-3}$	m	$0.3 \cdot 10^{-3}$	Typical observation, see the text
Z_h, case 2	≈ 2.28	$2.3 \cdot 10^{-3}$	m	$1.0 \cdot 10^{-3}$	Typical model, see the text

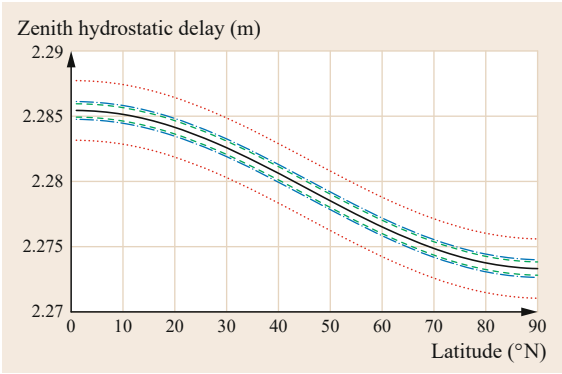

Fig. 38.5 The expected ZHD when a ground pressure of 1000 hPa is observed from the sea level (*solid black line*). The uncertainty in the ZHD caused by the uncertainties in the constants used in the conversion is indicated by the *green dashed lines*. The total uncertainty, when errors in the pressure observations of 0.2 hPa and 1.0 hPa are taken into account, is shown by the *blue dash-dotted* and the *red dotted lines*, respectively. All errors are assumed to be uncorrelated and added as root-sum-squared

uncertainty from the value of k_1 becomes equally important, resulting in a relative uncertainty of $0.3 \cdot 10^{-3}$. This means an uncertainty in the ZHD of less than 1 mm.

Finally, before leaving the subject of calculating the ZHD, it shall be noted that one additional uncertainty exists: the approximation of hydrostatic equilibrium. This approximation is good to one part in 10^4 [38.20]. The effect has been studied at two specific laser-ranging sites in mountainous areas. It was concluded that deviations from hydrostatic equilibrium may cause errors in excess of 1 cm, corresponding to 3 mm in the zenith direction, although it is an unlikely event [38.21].

From ZWD to IWV

The water vapor content, V, is defined as

$$V = \int_0^\infty \rho_v \, dh \,, \tag{38.4}$$

where ρ_v is the absolute humidity in g/m^3 and h is the height in m. An alternative parameter often used to describe the water vapor content of the atmosphere is the precipitable water (PW). This is a measure of the equivalent height of the column formed if all the water vapor is condensed and collected at the ground surface, that is, a PW value of 1 mm is equivalent to an IWV value of 1 kg/m^2.

Using the ideal gas law, we can instead use the partial pressure of water vapor e and the temperature T and obtain

$$V = \frac{1}{\rho_w R_w} \int_0^\infty \frac{e(h)}{T(h)} \, dh \,, \tag{38.5}$$

where ρ_w is the density of liquid water and R_w is the specific gas constant of water vapor.

We note that the expression for the ZWD is similar to

$$Z_w = 10^{-6} \left(k_2' \int_0^\infty \frac{e(h)}{T(h)} \, dh + k_3 \int_0^\infty \frac{e(h)}{T(h)^2} \, dh \right) \,, \tag{38.6}$$

where k_2' and k_3 are the constants determined from laboratory experiments of the refractivity. The values are given in Table 6.2 and (6.34) of Chap. 6.

We can combine (38.5) and (38.6) and express the IWV in the ZWD as

$$V = \frac{Z_w}{Q} \tag{38.7}$$

where

$$Q = 10^{-6} \rho_w R_w \left(\frac{k_3}{T_m} + k_2' \right) \,. \tag{38.8}$$

The parameter T_m can be estimated from the vertical profiles of the atmospheric temperature and the partial

pressure of water vapor

$$T_m = \frac{\int_0^\infty T(h)\frac{e(h)}{T(h)^2}\,dh}{\int_0^\infty \frac{e(h)}{T(h)^2}\,dh}\,. \tag{38.9}$$

It can be seen as a mean atmospheric temperature weighted by (e/T^2). Now, let us study the uncertainties introduced when calculating the IWV using the ZWD as an input. The relation between these two parameters is defined by (38.7), involving the density of wet air, the specific gas constant for wet air, k_2', k_3, and T_m. We note that T_m is the only one of these which will vary spatially and temporally.

In order to obtain T_m for a specific GNSS site, an obvious and accurate method is to use the vertical profiles of atmospheric temperature and humidity. Such profiles may be obtained from the reanalysis based on a numerical weather model. If such tools are not available, one may use a more simple relation. A linear relation was derived in [38.22]

$$T_m = 70.2 + 0.72\,T_s\,, \tag{38.10}$$

where T_s is the surface temperature in K.

A global study, using six years of data, of the uncertainty in T_m calculated from the surface temperature used results from numerical weather models and radiosonde observations [38.23]. It showed that the root mean square (rms) error was dominated by a mean bias. For example, the bias found when using (38.10) varied in the interval $\pm 3.5\%$. When the bias is removed, the remaining error was less than 0.5% over most of the globe.

We can also calculate values of Q using a model optimized for a specific region based on the annual variability in Q due to seasonal temperature variations. For Europe, such a model

$$Q = a_0 + a_1\theta + a_2 \sin\left(2\pi\frac{t_D}{365}\right) + a_3 \cos\left(2\pi\frac{t_D}{365}\right) \tag{38.11}$$

was derived from radiosonde data [38.24]. Here, θ is the site latitude in degrees and t_D is the decimal day of the year. Values for the coefficients a_0, a_1, a_2, and a_3 are given in [38.25] based on radiosonde data from 38 sites in Europe and spanning a period from 1989 to 1997. The resulting rms error in the IWV is of the order of 1.5%.

To conclude the discussion on how to estimate T_m, there can be calculations of statistical averages for sites, regions, or the whole globe. For a specific region or for a specific site, it is possible to develop a model including yearly variability which is often based on observational data, for example, from radiosondes. A more accurate method is to use an analysis based on a numerical weather model. There are several similarities to the technique of how to optimize the mapping function for a given site/region. The issue will be further discussed in the section on climate applications.

We can now assess the relative importance of the different contributions to the total uncertainty in the IWV. Summarizing the discussions above, we have:

- An uncertainty of 2–5 mm in the ZTD from the processing of GNSS data.
- An uncertainty in the ZHD, which is determined by the uncertainties of the parameters in Table 38.1 and illustrated in Fig. 38.5.
- The uncertainties introduced by the conversion from ZWD to IWV. These include uncertainties in k_2', k_3, the specific gas constant for water vapor R_w, and the mean temperature T_m. The temperature dependence of the density of liquid water is sufficiently small over the range of atmospheric temperature so that it can be neglected [38.26].

In order to compare the relative importance of all these contributions, a number of different assumptions about these uncertainties are made in Fig. 38.6. These plots show the uncertainties for a dry and cold, a temperate, and a hot and humid troposphere. We note that in a dry and cold troposphere, the IWV uncertainty is mainly caused by the assumed accuracy of 3 mm in the ZTD plus the assumed accuracy in the ground pressure observations. As the troposphere becomes warmer and more humid, the relative importance of the uncertainty in the conversion factor Q increases.

38.1.3 Applications to Weather Forecasting

Water vapor is an important parameter determining the state of the atmosphere. A general understanding can be obtained by studying the water cycle in the atmosphere. In short, it can be described as follows:

Water on the ground – in the oceans, lakes, streams, and vegetation – evaporates and transpirates into the atmosphere. It carries energy, which is released when the water vapor condenses into clouds. These clouds may form precipitation more or less immediately, or at a later stage when the atmospheric conditions cause the liquid drops formed to be large enough to fall back to the surface of the Earth.

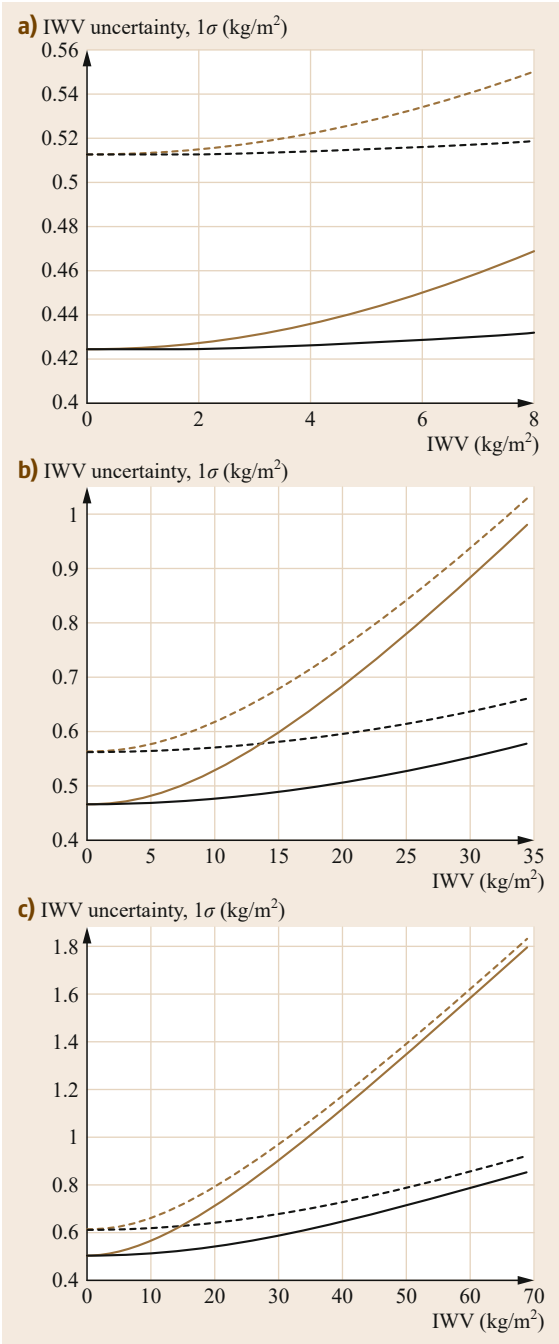

Fig. 38.6a–c The expected uncertainty in terms of one standard deviation in the IWV. Three different weather conditions are presented: cold ($T_m = 250\,K$, $Q = 7.26$, **(a)**), medium ($T_m = 275\,K$, $Q = 6.63$, **(b)**), and hot ($T_m = 300\,K$, $Q = 6.10$, **(c)**). Since the temperatures are strongly correlated with the absolute humidity in the atmosphere the chosen ranges for the IWV are different for different cases. In all cases we assume an uncertainty in the ZTD of 3 mm. We add an uncertainty due to the hydrostatic delay for two different uncertainties in the ground pressure: either 0.2 hPa (*solid lines*) or 1.0 hPa (*dotted lines*) and finally the uncertainty from the conversion from ZWD to IWV for two different uncertainties in the parameter Q: either 1.0% (*black lines*) or 2.5% (*light brown lines*). All errors are assumed to be one standard deviation, uncorrelated, and are added as root-sum-squared ◀

Knowledge about the amount of water vapor in the atmosphere is mainly important for short-term forecasts or nowcasting. The IWV is highly variable in space and time. For example, it may change by a factor of 2 in just a couple of hours due to moving mesoscale weather systems carrying different types of air masses in terms of temperatures and humidities. In order to be useful in weather forecasting, the IWV results must be available within a couple of hours, but the sooner the better.

Because warm and cold air masses often correlate strongly with the IWV, large-scale motions of mesoscale systems are easily tracked by ground-based networks. Distinct cold or warm fronts can be the cause of significant spatial and temporal gradients in the IWV above a GNSS site. Combining time series from many sites makes it possible to track such weather systems [38.27]. Such a spatiotemporal structure was assessed by an Empirical Orthogonal Function (EOF) analysis, where over 90% of the water vapor variability is explained using the first temporal eigenvector only [38.28]. For very dense networks and weather situations that are accurately described by a *frozen flow*, it has been shown that estimates of wind speed and wind direction can be made [38.29]. It shall, of course, be noted that this is an indirect method, and when the frozen flow hypothesis is not valid, the method will break down.

Large investments have been made in continuously operating reference networks for surveying and real-time kinematic (RTK) applications. Such networks are typically established on a national scale by government bodies, but also commercial networks exist. This means that not all data are openly available in real time which in practice means some restrictions on how data can be distributed for close to real time processing. An example is the EUMETNET GNSS Water Vapour Programme (E-GVAP). A snapshot of the status at a specific time is shown in Fig. 38.7. (EUMETNET is a group of European National Meteorological Services that provides a framework for co-operative programmes in the various fields of basic meteorological activities.)

In Germany, where many stations participate in the E-GVAP network, the receivers are distributed with

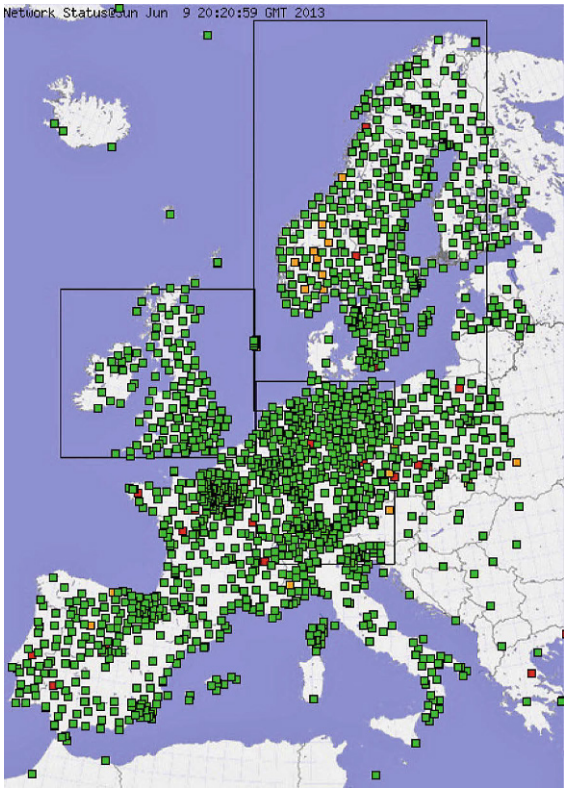

Fig. 38.7 The E-GVAP project is an example of a network of GNSS receivers consisting of several subnetworks where data processing is distributed to several centers. This example is from 2013 and the number of stations continues to increase (after [38.30])

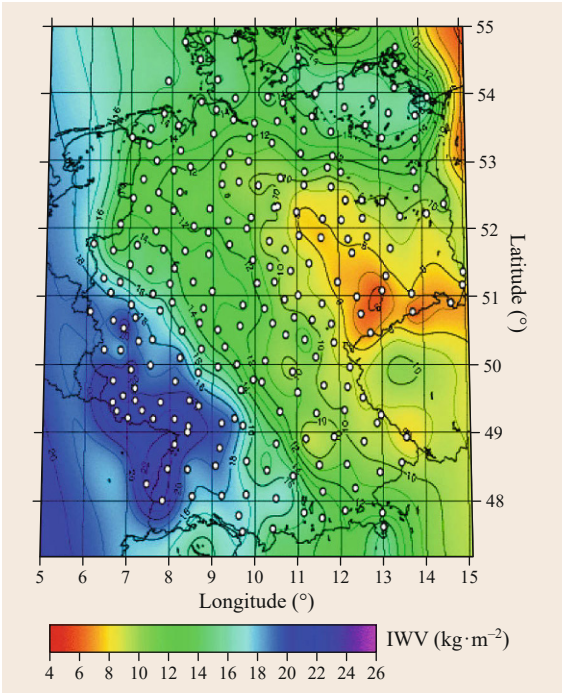

Fig. 38.8 The IWV over Germany on Feb. 28, 2010, 00:07 coordinated universal time (UTC), derived from ground-based GNSS stations. The white circles denote the locations of GNSS receiver sites (courtesy of G. Dick, GFZ)

a rather high spatial resolution and baseline lengths of the order of 40 km. An example of GNSS-based results of the IWV is shown in Fig. 38.8.

Assimilation of the estimated IWV was first considered when using GNSS data for weather forecasting. However, it was almost immediately realized that because the necessary information, in terms of pressure and temperature fields, is already available in the numerical weather model it is an advantage to instead assimilate the ZTD.

The method of three-dimensional variational data assimilation (3D-Var) is often used with a typical update period of 3 h. However, the four-dimensional variational data assimilation (4D-Var) method offers to benefit from the much higher temporal resolution of the GNSS results. The timing of the passage of weather systems and different dry and wet air masses is crucial for short-term weather forecasts [38.31].

There have been many assessments of the impact on the quality of weather forecasts when using GNSS data. Assimilation of ZTDs has, for example, shown improvements in precipitation and cloud cover forecasts (see [38.32] and [38.33], respectively).

A further refinement may be to assimilate slant delays [38.34]. These delays may be estimated by combining the ZTD with estimated linear gradients. An alternative in order to study small-scale variations in the atmospheric water vapor (without assimilation) is to apply tomographic methods to very dense ground-based networks. Having all GNSS receiving antennas on the ground will, however, imply a weak geometry for the inversion algorithms used in tomography. This can to some extent be compensated for by introducing constraints on the variability in the water vapor density between the different volume pixels defined and used in the estimation method [38.35, 36]. The geometry is, of course, improved if the receivers are located in a landscape where the height differences are large as this will directly yield differential IWV values for different atmospheric layers. Such studies have, for example, been performed on Hawaii [38.37].

In the future, one can imagine that the raw GNSS observations are assimilated, effectively meaning that the entire GNSS data processing is executed in the numerical weather model.

38.1.4 Applications to Climate Research

Water vapor in the atmosphere is of great relevance also for climate research because it is a very important parameter in the water cycle as well as an efficient greenhouse gas. An increase of 20% of the IWV in the tropics has a larger impact than a doubling of the carbon dioxide concentration [38.38].

One key question is to quantify the positive feedback due to an increase in the IWV. A study of both the short-term and the long-term feedback concluded that the time series of observed water vapor need to be longer than 25 years in order to accurately determine the effect [38.39]. The GNSS ground-based networks established in the mid-1990s will, hence, have the potential to be useful for such applications in the 2020s.

Within the Global Climate Observing System (GCOS), there is a specific international reference observing network called the GCOS Reference Upper Air Network (GRUAN). One component in GRUAN is ground-based GNSS observations in order to provide IWV time series at selected reference sites where several independent observing techniques are available [38.40].

We first present some examples of GNSS results focusing on different timescales: trends over decades, annual components, and diurnal components. These may be used for climate monitoring and for evaluating of climate models which concludes this first part of GNSS meteorology using ground-based networks.

Long-Term Trends

There is a demand for long and stable time series for monitoring and therefore there is a need to assess the uncertainty at an absolute level, or at least as a stability measure, over decades. Since errors in the empirically determined constants k_1, k_2, and k_3 will not influence the uncertainties in the observed trends, for this application, it is more appropriate to refer to requirements on the long-term stability than on the absolute accuracy.

The difficulty to estimate trends that are of the order of a few percent over decades is illustrated in Fig. 38.9. The variability is huge – not only on a day-to-day basis but also over the seasons and from one year to another. Therefore, it is important to note that estimates of linear trends by no means shall be expected to be identical for adjacent periods of several years.

In addition to the large variability in weather, an additional issue is change (controlled or uncontrolled) in the electromagnetic environment of the receiving antenna. Examples of such changes are installations of different types of antennas and radomes, as well as their orientation. For the case of estimating a trend in the vertical coordinate, when there are reasons to believe that the trend is constant over the length of the time series, one may choose to estimate an additional offset at the time of the intervention (see Fig. 38.10 and [38.41] for more details).

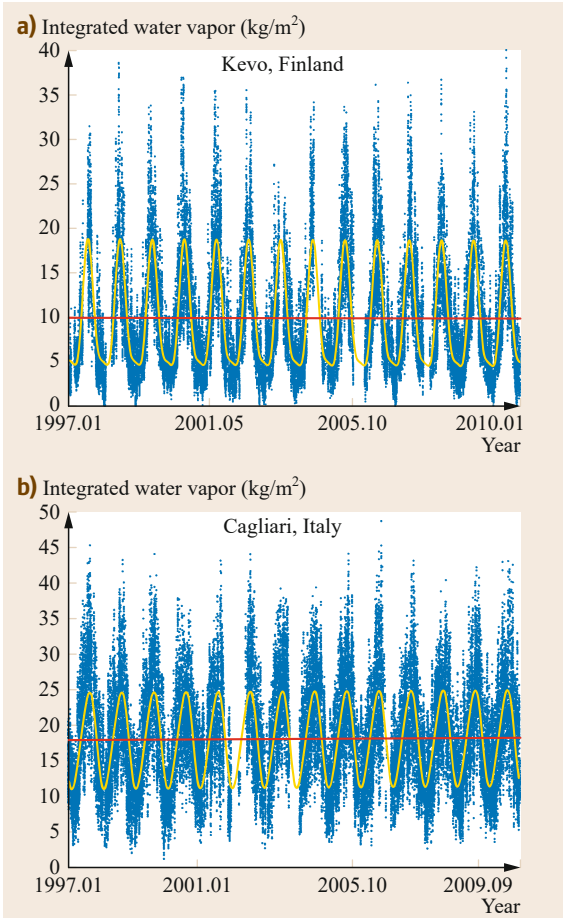

Fig. 38.9a,b Time series of the water vapor content at Kevo, Finland **(a)** and Cagliari, Italy **(b)**. A model including a mean value plus a linear trend (*red line*) and a seasonal component (*yellow line*) is fitted to the hourly estimates (*blue dots*)

As already mentioned, it is not reasonable to assume that a true trend in the IWV should remain constant over many years, in spite of the fact that an estimated linear trend is an obvious parameter to estimate as an indicator of a change in the climate.

A similar method was assessed in [38.42], where an effort was made to model the impact of a change of radome at Onsala, Sweden, on February 1, 1999. It was more reliable in this case to study the mean difference of the wet delay between the GNSS and the VLBI techniques and to apply the observed change in offset

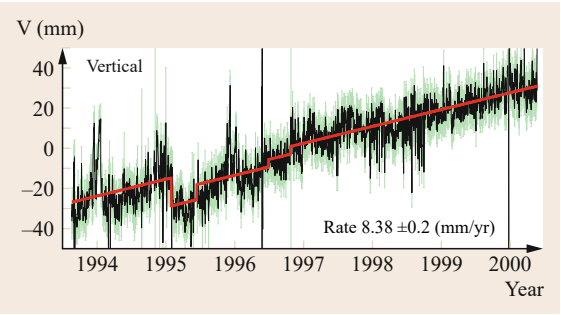

Fig. 38.10 Estimates of the vertical coordinate using GPS data from the station Sveg, Sweden (courtesy of Scherneck & Haas)

as a constraint when estimating a trend from the full time series, thereby indirectly using the VLBI technique as an independent data source to calibrate the absolute scale of the IWV from the GNSS data.

A possibility of handling false jumps in the IWV time series when no independent results are available could be to make use of the correlation between estimates of station coordinates and the propagation delay. This idea requires further studies.

Annual Components in the IWV

Annual components in the IWV show large differences over the globe caused by different weather patterns related to the seasons. Through continuously operating ground-based networks and a homogeneous processing, GNSS is a tool to continue such systematic studies. For example, 13 years of data from 155 globally distributed GNSS sites were studied in order to conclude that the large seasonal amplitudes occurred at mid latitudes [38.43].

Also, more local studies, with a higher spatial resolution, have been carried out. For example, a 10 year long period was studied using GNSS data from the Iberian peninsula in [38.44] and [38.45] revealed a systematic deviation in the southwest of Spain during the summers.

Diurnal Components in the IWV

The diurnal variability in the IWV is driven by the incoming solar radiation. Hence, it is more dominant in the equatorial region, and as we go away from the equator, the amplitude decreases and vanishes in the areas close to the poles. For the same reason, and because the absolute humidity typically increases with the temperature, it is also expected to be larger during the summer compared to the winter. The knowledge of its amplitude and phase can be a useful tool in order to assess the accuracy of numerical weather models used both for forecasting and in climate research.

In a global study using 1 year of data from 151 International GNSS Service (IGS) sites, diurnal amplitudes between 0.2 mm and 10.9 mm in the ZTD were observed [38.46]. This corresponds to approximately from less than 0.1 up to 1.7 kg/m^2. A similar study also using a US network [38.47] obtained similar results and also assessed the accuracy of three different reanalysis products.

In a study using 14 IGS sites in the equatorial region, diurnal amplitudes up to 3 kg/m^2 were observed [38.48]. The amplitudes were larger for sites that are not close to the sea, which is expected, in general, because of the lower diurnal variability of the temperature close to the sea compared to more inland areas.

It may be worth noting that the diurnal components at mid to high latitudes is hidden by the much larger moving mesoscale weather systems. This together with the fact that the diurnal variation of the solar radiation has a much smaller amplitude means that typically many years of GNSS data must be averaged in order just to detect the diurnal component [38.49].

Evaluation of Climate Models

We have already touched upon the application of using the GNSS data in order to evaluate numerical climate models for the trends, annual, and diurnal components in IWV time series.

An additional study that focused both on the validation of seasonal and interannual variations in the IWV was presented in [38.50]. The authors of this study found, in general, an agreement at the submillimeter level for the precipitable water in Europe and North America between GNSS and a numerical weather prediction model from National Centers for Environmental Prediction (NCEP). On the other hand, the model was found to underestimate the seasonal signal by up to 40% and 25% for the equatorial region and Antarctica, respectively.

In [38.51], a regional climate model was evaluated in terms of the IWV differences between GNSS observations and the climate model. It was found that a couple of GNSS sites showed large differences, which in turn were attributed to a cold temperature bias and an underestimate of the diurnal temperature range for the model in that area. It was also noted that the model produced a positive bias in the IWV at sites close to the sea (the surface tile of the model gridpoint has a water coverage $> 60\%$), possibly due to the fact that evaporation in the model has a too high influence on the IWV mean value for the gridpoint.

As mentioned several times already, climate studies require long-term averages. It therefore seems appro-

priate to note that so far the potential of ground-based GNSS has been demonstrated, but there is a limitation today on the studies that are meaningful due to the length of available time series. This situation will however improve over the years to come.

The next section will deal with the occultation geometry in GNSS meteorology. Thereafter, we will conclude the chapter by summarizing the GNSS applications for the remote sensing of the neutral atmosphere.

38.2 GNSS Radio Occultation Measurements

38.2.1 Introduction and History

On July 17, 1995 the U.S. Air Force announced

> *[...] that the Global Positioning System satellite constellation has met all requirements for Full Operational Capability.*

Already before this announcement on April 5, 1995 the LEO MicroLab-1 satellite was launched and recorded for the first time at all signals from setting GPS satellites, which tangentially traversed the Earth's atmosphere. The main purpose of these observations was atmosphere sounding using the innovative GPS RO technique within the GPS/MET(GPS/METeorology)-Experiment [38.52, 53].

GPS/MET was a real story of success. For the first time, globally distributed vertical profiles of atmospheric temperature, water vapor, and electron density were successfully derived from spaceborne GPS data. The GPS (or, more generally, GNSS) RO technique became reality as a new and innovative remote-sensing method. The properties of this calibration-free atmospheric limb-sounding technique (e.g., all-weather-capability, high accuracy, high vertical resolution, low-cost realization) promised to have a great potential for atmospheric and ionospheric research, numerical weather forecasts, space weather monitoring, and climate change detection [38.54].

Around 20 years later, it can be stated, that GNSS RO kept this promise and is widely recognized as an established atmospheric remote-sensing technique. A major and prominent example for this development is the beginning of the operational use of GNSS RO data to improve global numerical weather forecasts (e.g., [38.55, 56]). Figure 38.11 shows a schematic illustration of the GNSS observation geometry. A GNSS receiver aboard an LEO satellite tracks the signals (carrier-phase and amplitude) of an occulting GNSS satellite, that is, within the period directly before satellite *set* or before satellite *rise*. These are the occultation events and last typically 1–2 min for atmosphere sounding from the Earth's surface up to around 100 km. During these events, the signal goes through different vertical layers of the atmosphere and is modified in a characteristic way. By appropriate inversion of the time series of the signals during the occultation, vertical profiles of atmospheric parameters, as refractive index, temperature, or water vapor can be derived. GNSS RO can also be used to derive vertical electron density profiles, as described in more detail in Chapt. 40 of this book. A key observable is the bending angle α of the signal path from the occulting GNSS to the LEO satellite, which is assigned to the impact parameter a and the point of the closest approach of the signal path to the Earth's surface r_0. Additional LEO measurements from a referencing GNSS satellite and GNSS ground station data from the occulting and referencing satellite are used for the calibration of the atmospheric excess phase of the occultation measurements, which is the base for the bending angle derivation. More details are given in Sect. 38.2.2.

38.2.2 Basic Principles and Data Analysis

Derivation of the Atmospheric Excess Phase

The GNSS RO technique is based on precise dual-frequency (for ionosphere correction) phase measurements of a GNSS receiver in an LEO, which is tracking setting or rising GNSS satellites. Combining these measurements with the satellites' position and velocity information, the phase path increase due to the atmosphere during the occultation event can be derived. This phase path increase is called atmospheric phase delay or atmospheric excess phase, dA and the geodetic key observable of GNSS RO and its derivation here briefly reviewed.

The observed phase L for each frequency of the occultation link (see in Fig. 38.11 between occulting GNSS satellite and LEO) in units of meters can be written as

$$L = \rho + c(dt - dT) - dI + dA + \epsilon \,. \qquad (38.12)$$

Here, ρ denotes the true range between the transmitter and receiver taking into account the signal travel time, c is the velocity of light, dt and dT are the transmitter and receiver clock errors, respectively, dI and dA are the phase delays due to ionosphere and neutral atmosphere

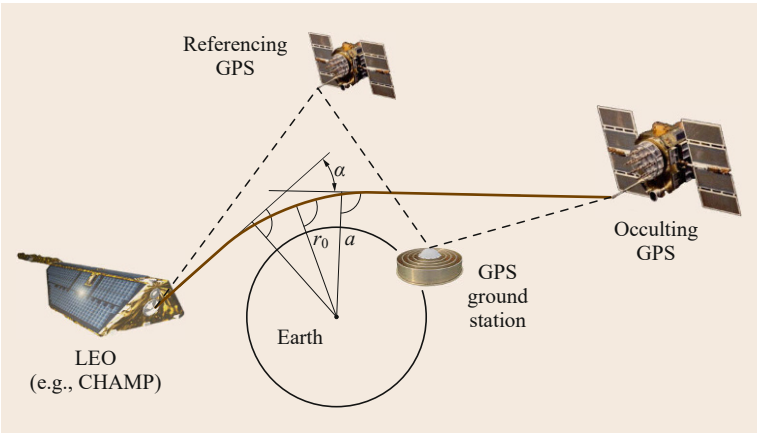

Fig. 38.11 The principle of GNSS RO measurements aboard a LEO satellite such as CHAMP (CHAllenging Minisatellite Payload). A key observable is the atmospheric bending angle α of the signal path from the occulting GNSS to the LEO satellite. Under assumption of spherical symmetry an impact parameter a can be assigned. LEO measurements from a referencing GNSS satellite and GNSS ground station (*dashed lines*) are used for calibration of the RO measurements.

along the ray path, respectively, and ϵ is a residual error composed of, for example, measurement noise and uncorrected multipath.

For the analysis of the GPS/MET and the initial CHAllenging Minisatellite Payload (CHAMP) measurements [38.52, 57], a double-difference technique was used to eliminate the GNSS transmitter and LEO receiver satellite clock errors: the signals from the occulting GNSS satellite were differenced with those from a reference GNSS satellite. These satellite measurements were synchronized with simultaneously recorded data provided by a fiducial ground network [38.58]. The corresponding observation geometry is depicted in Fig. 38.11.

The double difference,

$$\Delta\Delta L = (L_{\mathrm{CO}} - L_{\mathrm{CR}}) - (L_{\mathrm{GO}} - L_{\mathrm{GR}}) \,, \tag{38.13}$$

is formed from simultaneous CHAMP and ground station measurements of signals from both the occulting and the referencing GNSS satellite during an occultation (e.g., [38.58]). The subscripts C, O, R, and G denote CHAMP, occulting and referencing GPS satellite, and the ground station, respectively. The corrections of relativistic and light time effects have to be taken into account [38.59]. Equation (38.13) shows that in the double-difference method, both the transmitter clock errors dt_{O} and receiver clock errors dt_{R} cancel. While the double-difference method eliminates the satellite clock errors, other errors are introduced by the three auxiliary satellite links involved. These errors are uncalibrated atmospheric and ionospheric contributions and additional noise. Furthermore, for differencing with nonsynchronous receiving times of occultation and reference satellite, the ground receiver clock drifts and also multipath wave propagation at the ground station location have to be taken into account (e.g., [38.60]).

Due to the termination of Selective Availability (SA) on May 2, 2000, which reduced the apparent variations in the GNSS transmitter clocks by various orders of magnitude, and due to the higher stability of presently available LEO satellite clocks, the application of single- and even zero-differencing analysis techniques represents the current state of the art for GNSS RO data analyses [38.61, 62].

For example, the space-based single difference,

$$\Delta L = (L_{\mathrm{CO}} - L_{\mathrm{CR}}) \tag{38.14}$$

is the difference between phase measurements of CHAMP from the occulting GNSS, L_{CO}, and the referencing GNSS, L_{CR}, respectively. In this scheme, the GNSS satellite clock errors remain and need to be corrected for, what is feasible after the termination of SA even with the standard data products of the IGS. For GNSS RO satellites with ultra stable oscillators (USOs), as, for example, GRACE-A or Metop, even the forming of single differences is not required and the phase data of the occultation link L_{CO} can be directly used for the derivation of dA. With single and zero differencing, the level of random noise in dA should be lower and also systematic errors from the calibration links are avoided.

More details of the excess phase calibration are given in several publications, for example, [38.59, 61]. Figure 38.12 shows the atmospheric phase delay and the corresponding amplitude (signal-to-noise ratio, SNR) for a typical TerraSAR-X occultation measurement. Typically, occultation measurements for the neutral atmosphere (0–120 km altitude) last around 1–2 min, and the atmospheric excess phase is around 1 km in the vicinity of the Earth's surface.

Derivation of Vertical Atmospheric Profiles

The calibration of the atmospheric excess phase can be regarded as a geodetic task and is the basis for the

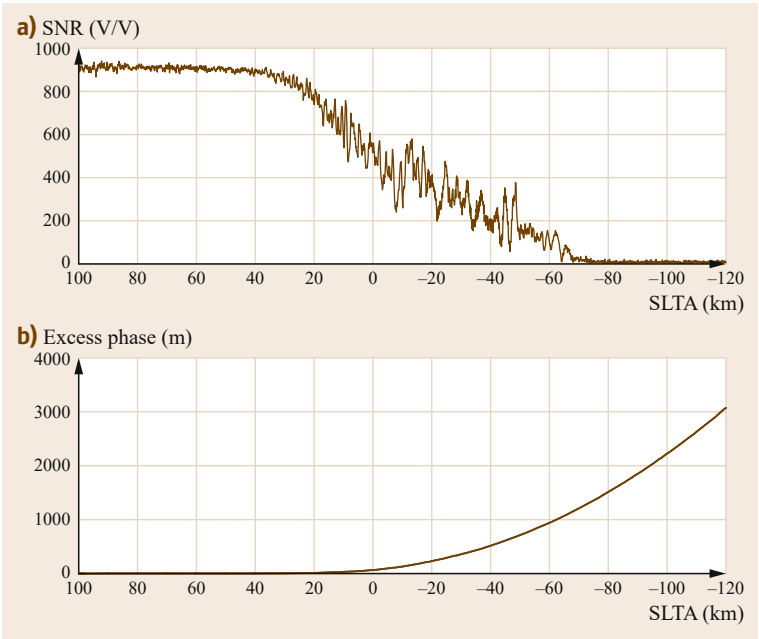

Fig. 38.12a,b Variation of the SNR **(a)** and the corresponding atmospheric excess phase **(b)** for a typical occultation event. SLTA indicates the Straight Line Tangent point Altitude. The plots characterize an occultation measurement of the TerraSAR-X satellite on February 18, 2012, 05:46 UTC, 79.6°N and 88.5°W (courtesy of F. Zus, GFZ)

mathematic-physical calculations to retrieve the vertical atmospheric profiles. The first step consists in the derivation of atmospheric bending angles, which are obtained from the time derivative of the atmospheric excess phase using the Doppler shift equation (e.g., [38.63])

$$f_\mathrm{d} = f_\mathrm{c}\left(\frac{c-(\boldsymbol{v}_2\cdot\boldsymbol{m}_2)n_2}{c-(\boldsymbol{v}_1\cdot\boldsymbol{m}_1)n_1}-1\right) . \tag{38.15}$$

In (38.15), $\boldsymbol{v}_{1,2}$ are the velocity vectors of GPS and LEO satellite respectively, $\boldsymbol{m}_{1,2}$ are the unit wave vectors and $n_{1,2}$ are the refractivity at the satellite positions as shown in Fig. 38.13. The Doppler shift f_d is related to the phase L by

$$f_\mathrm{d} = -\frac{f_\mathrm{c}}{c}\frac{\mathrm{d}L}{\mathrm{d}t} \tag{38.16}$$

with the carrier frequency f_c and the vacuum light velocity c. L can be expressed as

$$L = L_0 + dA_\mathrm{LO} \tag{38.17}$$

Thus, the Doppler shift f_d is represented by two terms

$$f_\mathrm{d} = f_{\mathrm{d}0} + f_{dA} \tag{38.18}$$

The first term in (38.18), $f_{\mathrm{d}0}$, is equal to the frequency shift in the absence of the atmosphere and depends on L_0. It can be calculated using the precise orbit information of the satellites (position and velocity). The second term, f_{dA}, depends on the time derivative of the measured atmospheric excess phase A_LO of the occultation link between GPS and LEO. The bending angle is (Fig. 38.13)

$$\alpha = \phi_1 + \phi_2 + \theta - \pi . \tag{38.19}$$

ϕ_1 and ϕ_2 are unknowns; thus, one more equation is needed to calculate both ϕ_1 and ϕ_2. Assuming local spherical symmetry of the refractivity $n = n(r)$, Snell's law applies

$$r_1 n(r_1)\sin\phi_1 = r_2 n(r_2)\sin\phi_2 . \tag{38.20}$$

Equations (38.16) and (38.20) are nonlinear and cannot be solved analytically. It can be solved with an iterative method, as, for example, described in [38.63]. Starting with some increment $\Delta\phi_2 = \phi_2 - \phi_{20}$ (ϕ_{20} is equal to ϕ_2 in the absence of the atmosphere and can be calculated with satellite's orbit information) with (38.20) the corresponding $\Delta\phi_1$ can be calculated. Then the vectors $\boldsymbol{m}_1$ and $\boldsymbol{m}_2$ are constructed. Applying (38.15) $\Delta f = f_\mathrm{d} - f_{\mathrm{d}0}$ is calculated and compared with the observed value f_{dA}. Depending on the deviation of Δf from f_{dA}, the increment $\Delta\phi_2$ is modified and the procedure is repeated until ϕ_1 and ϕ_2 for each sample and with (38.20) the appropriate α is found.

The ionospheric correction is performed by the linear combination of the bending angle profiles obtained for each individual signal frequency (e.g., GPS L1 and

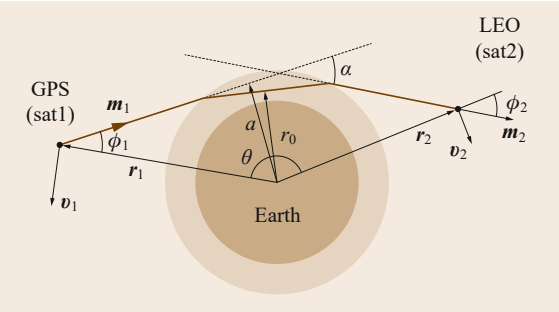

Fig. 38.13 Derivation of the bending angle α from the Doppler shift (a: impact parameter; r_0: radius of the point of closest approach). For details, see the text

L2; [38.64]).

$$L_C(t) = \frac{f_1^2}{f_1^2 - f_2^2} L_1(t) - \frac{f_2^2}{f_1^2 - f_2^2} L_2(t) \qquad (38.21)$$

$$\alpha_C(a) = \frac{f_1^2}{f_1^2 - f_2^2} \alpha_1(a) - \frac{f_2^2}{f_1^2 - f_2^2} \alpha_2(a) \,. \qquad (38.22)$$

The ionosphere correction in (38.22) avoids the effect of dispersion (L_1 and L_2 have separate signal paths), which forms the major error budget of (38.22) because the linear combination of the bending angles (38.22) is formed at the identical impact parameter for both frequencies.

Vertical profiles of the atmospheric refraction index n can then be retrieved from the ionosphere corrected bending angle profiles by the inverse Abel transform

$$n(r_0) = \exp\left(\frac{1}{\pi} \int_a^\infty \frac{\alpha(x)}{\sqrt{x^2 - a^2}} \mathrm{d}x\right) \qquad (38.23)$$

for the given point of the closest approach of the signal path to the Earth's surface r_0, bending angle α, and impact parameter a.

After accounting for ionospheric bending as described above, the atmospheric refractivity ($N = (n-1) \cdot 10^6$) is related to pressure (p in mbar), temperature (T in K), and water vapor pressure (p_w in mbar) via the *Smith–Weintraub* equation [38.65]

$$N = 77.6 \frac{p}{T} + 3.73 \cdot 10^5 \frac{p_w}{T^2} \,. \qquad (38.24)$$

For dry air, the density profiles are obtained from the known relationship between density and refractivity. Pressure and dry temperature

$$T_d = 77.6 \frac{p}{N} \qquad (38.25)$$

are obtained from the hydrostatic equation and the equation of state for an ideal gas. There are numerous publications, describing these retrieval steps in very detail, for example, [38.54, 60, 66].

When water vapor is present, additional information is required to determine the humidity and density from refractivity profiles, due to the joint contribution of the dry and wet term to the refractivity in (38.24). Temperature profiles from operational meteorological analyses (e.g., of the European Centre for Medium-Range Weather Forecasts, ECMWF) are used to derive humidity profiles from the calculated refractivity in an iterative procedure [38.67]. This algorithm suffers from a high sensitivity to even small errors in the analyses temperatures, resulting in large uncertainties of the derived water vapor profiles [38.68]. More elaborate retrieval methods are based on the estimation of both temperature and humidity in parallel including the error characteristics of the measurement and the *background* information, which is usually obtained from meteorological analyses (optimal estimation, for example, [38.69, 70]). These methods show an increased potential for obtaining water vapor profiles with high accuracy.

By way of example, Fig. 38.14 shows vertical profiles of dry temperature and water vapor derived from a TerraSAR-X occultation measurement. The deviation (cold bias) of the dry temperature from the temperature below 10 km altitude is clearly seen and most obvious below 3 km, where the major part of the atmospheric water vapor is present. The magnitude of this deviation can itself be regarded as a measure for the atmospheric water vapor. It is noted that the key observables for the assimilation of RO data into forecast models are the bending angles or refractivities, rather than temperature and water vapor. The separation of these observables into dry and wet contributions, which finally provides the temperature and water vapor, is performed during the model analysis process using additional data from other observing systems. Also, for several climate change-related investigations, bending angle and refractivity data are used (e.g., [38.71]).

A major challenge in the GNSS RO data analysis is the parameter retrieval in the lower troposphere. Sharp refractivity gradients, mainly due to irregular water vapor distribution, complicate the proper signal tracking and the assumption of geometrical optics for analysis cannot be applied in contrast to higher altitudes. The application of the open-loop GNSS signal tracking technique as well as the development and application of advanced occultation data analysis techniques, however, brought significant progress during the last decade [38.72–76]. Another recent challenge is the data analysis in the upper stratosphere, where the occulta-

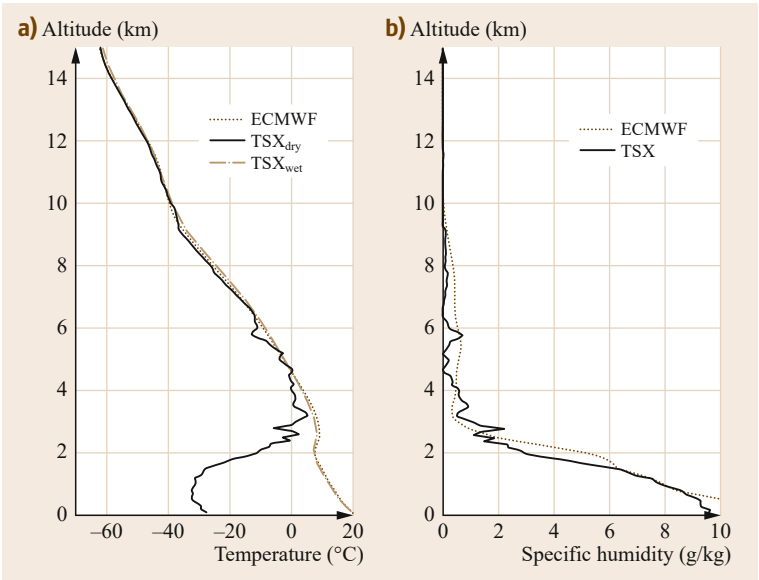

Fig. 38.14a,b Typical vertical dry (*black*) and wet (*light brown*) temperature **(a)** and water vapor profiles **(b)** derived from GNSS RO data. The example is from the TerraSAR-X (TSX) mission (July 19, 2010, 02:47 UTC, 31.43°N 145.67°E). Only the troposphere is shown. The RO data are compared with corresponding values from ECMWF analyzes (*brown dotted line*) (courtesy of S. Heise, GFZ)

tion signal is very weak and measurement errors (e.g., ionosphere) start to dominate the neutral atmosphere signal [38.66, 77].

38.2.3 Occultation Missions

A nearly complete and recent (as of 2016) list of satellite missions with GNSS RO instruments is given in [38.78]. Here, we give more details on selected missions of most importance for the development of the GNSS RO technique.

Initial GNSS RO data were recorded within the GPS/MET experiment aboard the MicroLab-1 satellite from 1995 to 1997 [38.52, 53]. However, the analysis of these data was primarily focused on the four *prime-times*, that is, periods of 2–3 weeks, when an anti-spoofing (A/S) encryption of the GPS signals was disabled and MicroLab-1 was oriented so that GPS satellites were occulted in the aft or anti-velocity direction toward the Earth's limb.

The German CHAMP satellite, launched on July 15, 2000 provided for the first time continuous and also near-real-time GPS RO data [38.57, 79]. These were especially used for various assimilation studies to investigate the potential improvement of RO data to numerical weather forecasts [38.80, 81]. In addition, CHAMP provided the first long-term set of GPS RO data covering the 2001–2009 period. In view of its high precision, it was used for initial climate-change-related investigations [38.82–84]. Furthermore, it triggered an international comparison of analysis results from different RO processing centers to define the structural uncertainty of GNSS RO data [38.85–87]. The CHAMP RO experiment can therefore be regarded as a big success and as a forerunner for several succeeding missions. However, the daily number of available occultation measurements was limited to about 150.

Gravity Recovery And Climate Experiment (GRACE) is a US/German twin-satellite mission with focus to the detection of climate-relevant long-term variations of the Earth's gravity field determination, which was launched on March 17, 2002. The two spacecraft are equipped with the same *BlackJack* GPS RO flight receiver provided by Jet Propulsion Laboratory (JPL) as CHAMP. Continuous GPS RO measurements were activated on May 22, 2006 aboard the GRACE-A satellite [38.79], which provides around 130 near-real-time occultation profiles until today (as of end 2015). Recently, the GRACE Follow On (GRACE-FO) mission was confirmed, which is foreseen for launch in 2017 and will also include a GNSS-RO instrument according to the current planning.

A breakthrough for the number of daily occultations and for improved data quality in the lower troposphere was the launches of the U.S./Taiwan six-satellite-constellation FormoSAT-3/COSMIC (April 15, 2006; [38.55]) and of the two European Metop satellites (October 19, 2006 [38.88] and September 17, 2012). FormoSAT-3/COSMIC initially provided more than 2000 occultations daily in an open-loop tracking mode for better data quality in the lower troposphere. By 2013, the number of daily RO measurements had dropped to roughly half that value, since the nominal life time of the mission was reached and several satellites exhibit technical problems. Both Metop satellites together provide continuously and with high reliabil-

ity more than 1200 daily occultations. In addition, the German twin-satellite constellation TerraSAR-X (launched June 15, 2007) and TanDEM-X (launch June 21, 2010) provides a unique set of parallel occultation measurements [38.89] to investigate the accuracy potential of the GNSS RO technique in more detail. Data from TerraSAR-X are also provided in near real time for operational use in numerical weather forecasts.

The successor of the FormoSAT-3/COSMIC mission FormoSAT-7/COSMIC-2 is foreseen to be launched in 2016. This 12-satellite constellation will provide multi-GNSS LEO data (GPS, GLONASS, Galileo) from two different orbital inclinations. Six satellites are planned to be launched into low-inclination orbits in early 2016, and another six satellites into high-inclination orbits in 2018. This configuration will improve the global coverage of the GNSS RO data, especially in the Tropics. The GNSS RO payload, named TGRS for TriG (Tri-GNSS) GNSS RO System, is being developed by NASA's JPL and will be capable of tracking up to 12 000 high-quality profiles per day once both constellations are fully deployed. The third satellite of the Metop series will be launched in 2018. The planning for the follow-on system of the current EUMETSAT POLAR SYSTEM (EPS) includes also considerations for GNSS RO measurements. The EPS can be expected in the 2020 time frame.

In addition to these large and operational missions, there are several smaller international missions, which are in more detail overviewed in documents, generated by the International Radio Occultation Working Group (IROWG, [38.90]). The IROWG was established as a permanent Working Group of the Coordination Group for Meteorological Satellites (CGMS) in 2009 as part of the activities of the World Meteorological Organization (WMO). The IROWG serves as a forum for operational and research users of RO data.

Another RO-related activity is CICERO (Community Initiative for Continuous Earth Remote Observation), which acts as a commercial provider of RO data. CICERO plans to launch a demonstration satellite in 2016 followed by an operational six-satellite constellation (CICERO-I) in the same year. Each satellite is foreseen to provide more than 900 GPS occultations per day.

CICERO-2, the planned extension up to 24 satellites by 2019, will offer enhanced performance with GPS/GLONASS/Galileo-enabled receivers. It potentially will provide more than 1600 occultations per day from each satellite.

38.2.4 Occultation Number and Global Distribution

Figure 38.15 shows the number of daily occultations from the six-satellite FormoSAT-3/COSMIC and Metop-A/B missions since the beginning of 2009. The maximum number of daily FormoSAT-3/COSMIC measurements was reached in early 2009 with up to 2500 profiles. At that time, the mission had already accomplished the nominal lifetime of three years. Nevertheless, it provided up to 2000 profiles daily even seven years after launch. The decreasing number of daily profiles and its quite large variation is associated with increasing technical problems of the satellites, which are already in orbit more than double of the nominal lifetime. The number of RO measurements, provided by both Metop satellites, is very stable, and around 1400 profiles daily are operationally available in near-real time.

The number of daily vertical profiles available from GRAS is before quality control, while the FormoSAT-

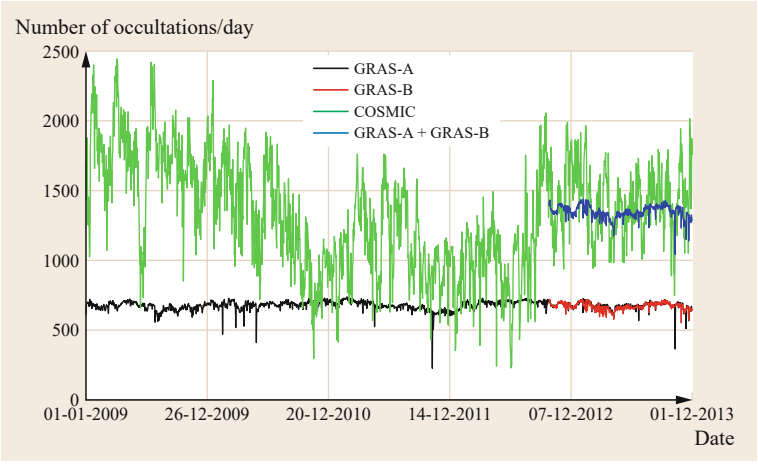

Fig. 38.15 Daily number of GNSS occultation measurements from GRAS-A (*black*), GRAS-B (*red*) and FormoSAT-3/COSMIC (*green*) between January 1, 2009 and December 1, 2013. The sum of the GRAS-A and -B data is indicated by the *dark blue line* (courtesy of A. von Engeln, EUMETSAT)

3/COSMIC numbers are after quality control. Typically, about 5–10% of the GRAS data are removed in quality control in the assimilation process of the weather services. Each of the GRAS receivers provides an almost constant number of daily occultations of around about 650–700. Some longer term variations are driven by the availability of GPS satellites for occultations, the short spikes are caused by, for example, loss of satellite data downloads or instrument updates.

Currently (as of end 2016), also GRACE-A and TerraSAR-X provide near-real-time RO data, but the daily number of around 150 measurements per satellite is much lower compared to Metop and FormoSAT-3/COSMIC.

A key property of the GNSS RO technique is the global coverage of the measurements, but the distribution is not uniform and depends mainly on the orbital geometry of the GNSS and the LEO satellites. As an example, Fig. 38.16 shows the global distribution of RO measurements from the FormoSAT-3/COSMIC mission (LEO orbit inclination $\approx 70°$). The figure is based on about 4.2 millions RO profiles obtained between 2007 and 2012. The spatial distribution is global and nearly symmetric with respect to the Equator but not equally distributed. Most significant are the variations with latitude from ≈ 800 occultations per pixel (Equator) or even lower in the Polar regions to ≈ 2500 at 25 and 50° N/S in the mid-latitudes.

The orbit inclination of the LEO satellite is a key parameter to modify the global distribution of the RO measurements. Low-inclination LEO orbits will result in higher occultation density in the Equator region, which is of major interest for the prediction of severe weather events such as typhoons. Therefore, the first six satellites of the 12 satellite FormoSAT-7/COSMIC-2 constellation (Sect. 38.2.3) will be deployed in a 20° inclination orbit. This will allow a higher equatorial occultation density compared to its predecessor mission. Near-polar orbiting LEO satellites (e.g., CHAMP, GRACE, Metop) exhibit a similar occultation distribution as shown in Fig. 38.16, but with more data available in the Polar regions (not shown here).

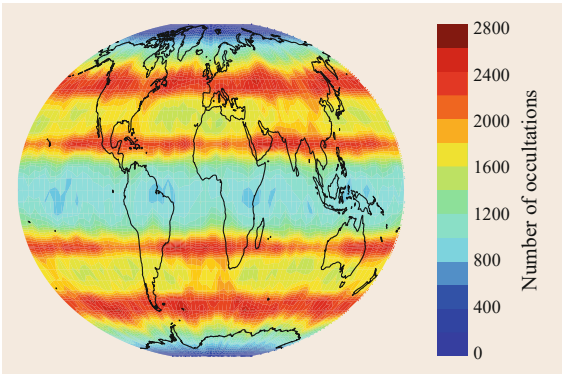

Fig. 38.16 Global distribution of GNSS RO data from the FormoSAT-3/COSMIC mission. The plot is based on about 4.2 million measurements, obtained between 2007 and 2012. The colors indicate the number of occultations per $5 \times 5°$ lat/lon grid cell (courtesy of C. Arras, GFZ)

38.2.5 Measurement Accuracy

Numerous validation studies were performed throughout the last years to evaluate the quality of the various occultation missions (e.g., [38.52, 55, 79, 88, 89, 91]). The vertical profiles of refractivity, temperature, and water vapor were validated with data from different meteorological analyzes and radiosondes. In addition, co-located RO profiles, observed from two different satellite platforms, were compared [38.89, 92]. The results indicate that especially temperatures in the upper troposphere lower stratosphere (UTLS) region agree well with the analyses and sonde data.

Between approximately 8 and 25 km altitude, that is, in the UTLS region, mean temperature deviations are ≤ 1 K, and rms errors fall within the 1–2 K range. Also, only very small biases of about $\pm 0.1\%$ and rms uncertainties of $\leq 0.5\%$ are observed for the refractivity (see, for example, Fig. 38.17 for TerraSAR-X). The deviations at these heights could be either due to analysis/sonde data or the RO retrievals.

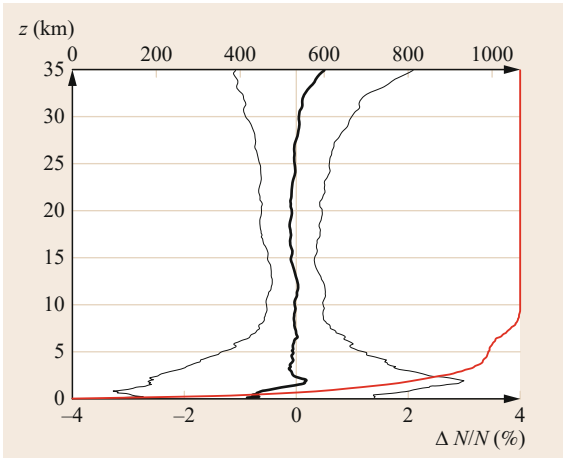

Fig. 38.17 Statistical comparison of refractivity profiles from TerraSAR-X with corresponding ECMWF data between November 26 and December 2, 2011. *Thick* and *thin black line* indicate bias and rms $(1-\sigma)$, the *red line* shows the number of compared data versus altitude (courtesy of F. Zus, GFZ)

A negative refractivity bias and significant loss of observations in the lower troposphere, especially at low latitudes, are observed in the RO retrievals and were in focus of numerous scientific studies, for example, [38.72–76]. One reason for this was found to be the application of the so-called phase lock loop (PLL) tracking mode of the occultation receivers of the early RO missions, such as GPS/MET or CHAMP. In the PLL mode, the phase of the RO signals is modeled (projected ahead) by extrapolating the previously extracted phase. This technique works well for standard GNSS observations (single-tone signals with sufficient SNR), but often fails for the occultation-geometry-like observations in the moist lower troposphere. Here, multipath propagation causes strong phase and amplitude fluctuations, which results in significant errors of the extrapolation-based phase model, a loss of SNR and finally loss of lock of the occultation signal. For this reason, the PLL mode does not allow in many cases a penetration of the occultation signals deep into the troposphere and is also the reason for systematic tracking errors. PLL mode receivers are also limited to the tracking of setting occultations only. An alternative tracking technique, open-loop (OL), that is, the raw sampling of the complex signal, was already applied to the data analysis of the planetary occultations and that also allows us to analyze rising occultation events [38.93]. However, a raw sampling of the signal is practically not feasible for routine GNSS RO sounding. Therefore, a model-based OL-tracking technique (e.g., [38.73]) was developed for the application in the moist troposphere for both rising and setting occultations and is used for several recent missions, for example, FormoSAT-3/COSMIC. In addition to these improvements of the occultation signal tracking, also the wave-optics-based retrieval techniques for the data analysis in the lower troposphere were improved during the years (e.g., [38.74–76, 94]).

The increased deviations above ≈ 25 km are also in the focus of recent investigations by RO and analysis specialists (e.g., [38.77]). On the one hand, GNSS RO retrievals become more difficult at these altitudes due to very small atmospheric excess phases; on the other hand, the analyses and the radiosondes exhibit problems at these altitudes.

The TerraSAR-X and TanDEM-X tandem satellite configuration (mean distance ≈ 20 km) provided for more than one year continuously vertical profiles at close quarters, recorded from different satellite platforms. This is a unique data set to investigate the accuracy potential of the RO technique and to determine its precision. Figure 38.18 shows a statistical comparison of corresponding refractivity profiles [38.89].

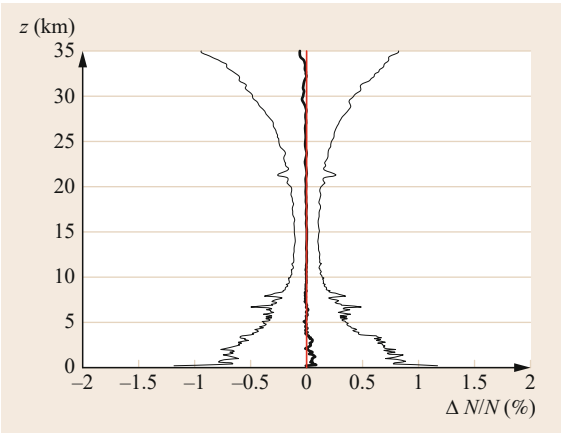

Fig. 38.18 Statistical comparison of the corresponding refractivity profiles from TerraSAR-X and TanDEM-X between November 26 and December 2, 2011. *Thick* and *thin black lines* indicate bias and rms, the *red line* indicates no deviation (courtesy of F. Zus, GFZ)

Nearly no or only an insignificant bias at the lower troposphere and above ≈ 30 km can be observed. The standard deviation is $\approx 0.1\%$ in the UTLS, $\approx 0.5\%$ in the lower troposphere, and above ≈ 30 km. These findings are in very good agreement with those in [38.92] for co-located FormoSAT-3/COSMIC profiles during the deployment phase of this multisatellite mission.

It is only briefly noted here that the high precision of the GNSS RO data is a valuable property to calibrate other satellite data from microwave sensors, which are widely used for global weather forecasts [38.95].

38.2.6 Prospects of New Navigation Satellite Systems

Similar to other GNSS applications, the availability of new navigation satellite systems (such as Galileo, BeiDou, and QZSS), along with the impressive renaissance of GLONASS and the modernization of GPS, will also be of great benefit for GNSS RO science and technology. GNSS RO will obviously profit from the significantly increased number of transmitting satellites. Even a single-satellite mission could potentially increase the number of daily occultation observations by a factor of 3 or 4, compared to only GPS. Besides this quantitative aspect, the new GNSS signal structures exhibit various advantages for the data quality of future RO missions. One example is the use of a third carrier frequency for improved ionospheric correction and better RO data quality in the stratosphere (Sect.38.2.5). An initial summary on the prospects of the new GNSS for RO is given in [38.96].

38.2.7 Weather Prediction

The highlight of the GNSS RO applications and the breakthrough for its acceptance as an established atmospheric remote-sensing technique was the start of the operational use to improve global weather forecasts. Forerunner for this development was the German CHAMP satellite, which has been providing continuous near-real-time GNSS RO data since 2003. The average delay between the measurement and corresponding provision of globally distributed vertical atmospheric profiles was reduced from 5 h in 2003 to around 2 h in 2006 mainly by the implementation of optimized precise orbit determination procedures for CHAMP. These near-real-time data from GFZ were used by the leading forecast centers to develop appropriate assimilation techniques and to investigate and quantify the impact of the RO data on the forecasts [38.81]. Currently, the RO data are routinely used by the world-leading weather centers to improve their global numerical forecasts.

Several NWP (Numerical Weather Prediction) centers have reported a positive forecast impact with GNSS RO data (e.g., [38.80, 97–99]), despite the fact that the RO data numbers are low when compared with those of satellite radiances (major part of satellite data used) that are assimilated. For example, ECMWF assimilates around 10 million of conventional and satellite observations per 12 h period, of which 90% are satellite radiance measurements, and only around 2% are GNSS RO-bending angles. The main GNSS RO impact is seen for upper-tropospheric and stratospheric temperatures. The GNSS RO measurements are beneficial because they provide complementary information to the satellite radiance measurements. Compared with satellite nadir sounders, the GNSS RO measurements have excellent vertical resolution and do not require bias correction, so they *anchor* the bias correction applied to satellite radiances and help identify NWP model biases [38.100].

Figure 38.19 shows the historical begin of the assimilation of GNSS RO data from FormoSAT-3/COSMIC, CHAMP, and GRACE-A on December 12, 2006. The major information is the reduction/elimination of the ECMWF bias in the background and analysis temperature (≈ 0.2 K and ≈ 0.4 K) and geopotential height (5–10 m) of the 100 hPa pressure level compared to radiosonde data, which can be regarded as truth at these altitudes.

38.2.8 Climate Monitoring

RO observations are well suited for establishing a stable, long-term record required for climate monitoring (e.g., [38.82, 101, 102]). Key properties for this application are: global coverage, high accuracy, high vertical resolution, and independence from weather. Most important, however, is that the fundamental RO obser-

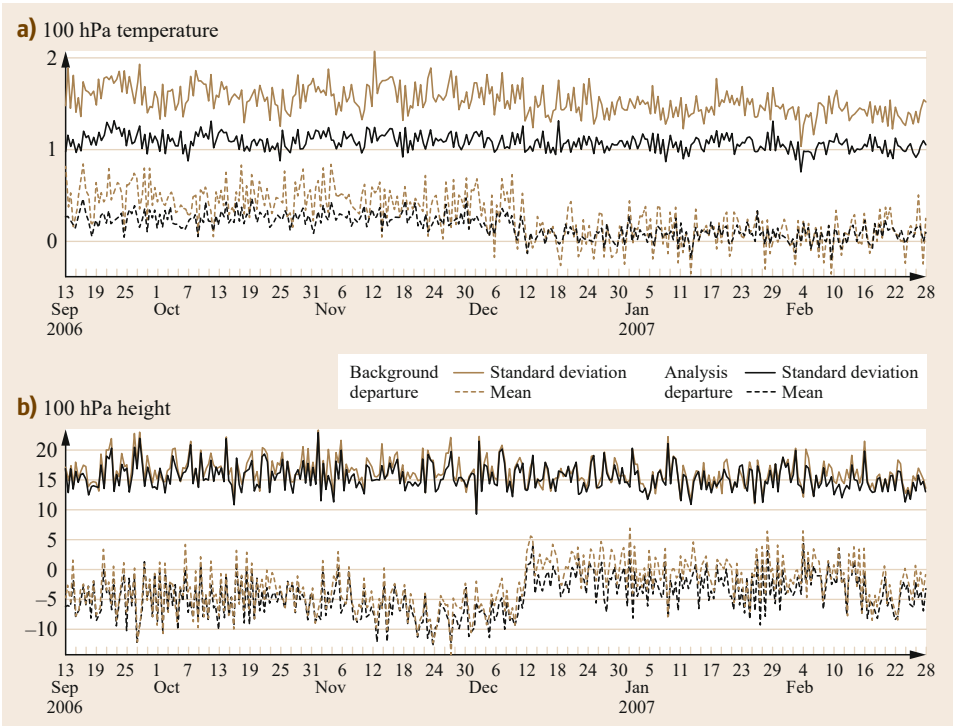

Fig. 38.19a,b Time series of the mean and standard deviation of the ECMWF operational background departures and analysis departures for **(a)** temperature and **(b)** geopotential height radiosonde measurements at 100 hPa in the southern hemisphere. GNSS-RO was introduced on December 12, 2006 (courtesy of S. Healy, ECMWF)

vation is a measurement of time (determination of the signal travel time), which is performed by atomic clocks with unequaled accuracy and stability. During an occultation, the GNSS receiver measures the change in the flight time of the signal transmitted by the occulted GNSS satellite. The clocks aboard the GNSS transmitters remain synchronized to the most stable atomic clocks on the ground. The clock in a GNSS receivers aboard an LEO satellite is synchronized, using the signals from up to 10 nonocculted GNSS transmitters in view and is thus tied to the stable ground-based GNSS time as well. Therefore, an extremely accurate measurement of the signal flight time with long-term stability can be achieved. Because the fundamental observation is a measurement of time, RO is a promising technique for climate monitoring.

The detection of climate trends is enormously important, especially because of their huge social and economical consequences, but there is presently no atmospheric instrument that can meet the stringent climate monitoring requirements of 0.5 K accuracy and 0.04 K decade^{-1} stability [38.102].

Global Temperature Trends

The upper troposphere and lower stratosphere (UTLS) are the key regions of the atmosphere with important links to the stratosphere–troposphere exchange as well as climate research. The determination of the UTLS temperature and tropopause (TP) height trends is crucial for the monitoring of climate-change processes (Sect. 38.2.8). Global high-resolution temperature observations in the UTLS region are only available from GNSS RO data. Here the CHAMP mission has generated the first long-term RO data set (2001–2008) that is continued with data from other mission (GRACE, FormoSAT-3/COSMIC, MetOp, TerraSAR-X). The UTLS region is also the vertical atmosphere region, where GNSS RO exhibits the highest accuracy (Sect. 38.2.5), another important property for the use in UTLS climate studies.

A global pattern of atmospheric temperature trends between 5 and 25 km is shown in Fig. 38.20. The figure was derived from CHAMP, GRACE-A, and TerraSAR-X GPS RO data between 2001 and 2013. The TP altitude is indicated with a white line. A slight overall warming in the upper troposphere (above 5 km to the TP) can be observed with largest values in the subtropical region of the southern hemisphere (SH). In the lower stratosphere from the TP up to 25 km predominant negative temperature trends (cooling) are detected. The equatorial TP region and the lower SH stratosphere reveal warming [38.82, 83, 103].

The results of these studies indicate the great potential of the very precise GNSS data to monitor even

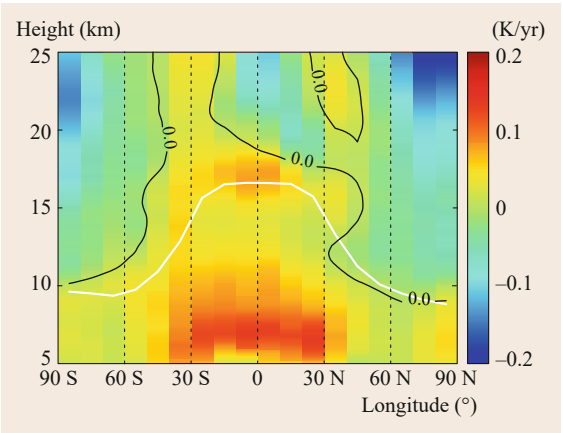

Fig. 38.20 Global temperature trends in the upper troposphere and lower stratosphere based on CHAMP, GRACE, and TerraSAR-X GPS RO data (2001–2013). The *solid white line* denotes the mean TP height (courtesy of T. Schmidt, GFZ)

small atmospheric temperature trends. This is also one reason for the current use of GPS RO data to validate a new model system for of mid-term climate forecast, which is, for example, currently developed in Germany.

To ensure a high data quality, especially for the RO climate applications, the international RO science community started in 2009 an important activity. RO products from different processing centers are compared regularly for the determination of the structural uncertainty in climate data records and the stability of trends (Fig. 38.21). These multicenter-based results ensure a high quality of the RO data analysis and provide more complete and reliable climatological information as derived from the results of only one center [38.85, 86].

The Tropopause: Indicator for Climate Change

The TP region separates the troposphere and stratosphere that have fundamentally different characteristics with respect to chemical composition and static stability. Therefore, the determination of TP parameters, such as altitude or temperature, on a global scale is an important goal for many branches in atmospheric research [38.104]. With regard to the current climate change discussion, TP parameters have received more attention in recent years since they are used to describe climate variability and change. The global mean TP altitude shows an increase in re-analyses and radiosonde observations over the last decades and seems to be a more sensitive indicator for climate change than the Earth's surface temperature [38.105]. Another ap-

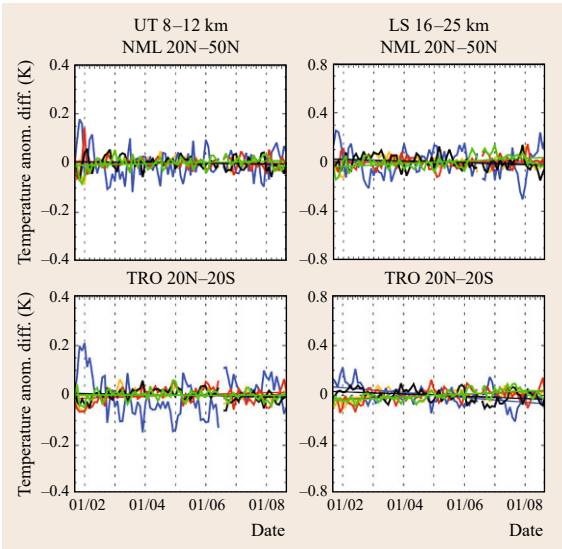

Fig. 38.21 Structural uncertainty in RO temperature records from different processing centers: DMI Copenhagen (*yellow*), GFZ Potsdam (*blue*), JPL Pasadena (*red*), UCAR Boulder (*black*), and WEGC Graz (*green*). Shown are difference time series of temperature anomalies for each center (with respect to the all-center mean) for the upper troposphere (left) and the lower stratosphere (right), for northern mid-latitudes (top) and the tropics (bottom). The overplotted difference trends are close to zero and indicate the stability of the RO data record (courtesy of A. Steiner, Wegener Center)

plication area of TP studies deals with the role of the TP region in the stratosphere–troposphere exchange. In this context, multiple tropopauses or TP break regions are important because in these regions most of the exchange processes take place (e.g., [38.106]).

One important data source for the determination of TP parameters is radiosondes. Despite good vertical resolution of the radiosonde data, global coverage is impossible. In contrast, the RO technique offers both global coverage and good vertical resolution as well and is therefore of particular relevance for detailed TP studies. First GNSS RO results for the tropical TP region were already published based on GPS/MET data [38.107, 108]. An example for the TP-related investigations is shown in Fig. 38.22 based on the investigations described in [38.109]. A significant increase of the global mean TP height of about 6 m/year between 2001 and 2011 was found associated with a warming in the upper troposphere. This could be an indication for a warming (extension) of the entire TP (connected with the cooling of the stratosphere), but longer data sets are needed to get more confidence of these early GNSS RO results for climate change research.

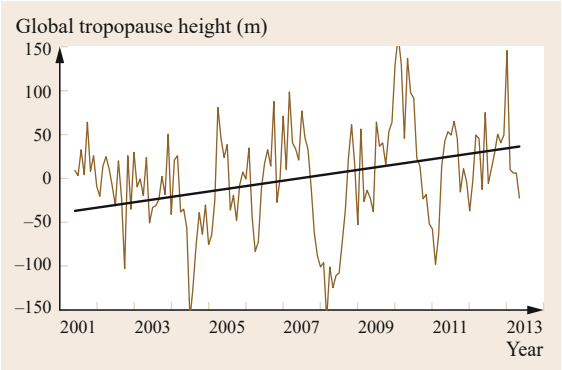

Fig. 38.22 Global TP height trend (*black line*) based on CHAMP, GRACE, and TerraSAR-X GPS RO data (2001–2011). The *brown line* indicates the monthly mean global TP height, derived from these RO missions (courtesy of T. Schmidt, GFZ)

Gravity Waves

Another important and climate change detection related application of the GNSS RO data is the derivation of atmospheric wave parameters on a global scale. Most relevant in this respect are gravity waves (GWs, wave phenomena, where the force of gravity tries to restore equilibrium), which play an important role for the general atmospheric circulation due to the related transport of energy and momentum between different regions of the atmosphere. Therefore, their analysis is of great interest for local weather forecasts and global climate modeling.

Early studies were initiated with GPS/MET data [38.110] and focused on vertically propagating waves. Recent studies (e.g., [38.111]) use much larger databases from multisatellite constellations and indicate the potential to derive also horizontal wave properties. Figure 38.23 shows the momentum flux (MF) distribution for July as a mean of 4 years (2007–2010) within the altitude range of 20–25 km. High values of MF along the southern Andes and at the east of the Andes are due to strong steady west wind crossing the mountains in that region. In the tropical regions, the high gravity wave activity, which induces high values of MF, is due to intense convection. The northern hemisphere is rather quiet in the local summer, therefore showing low MF values (Fig. 38.23). Atmospheric waves, for example, tides, can also be detected in spatiotemporal signatures of ionospheric irregularities (Sporadic E layer), detected using the GNSS RO technique [38.112].

The Planetary Boundary Layer

Recently scientists recognized more and more importance of the dynamics of the planetary boundary layer

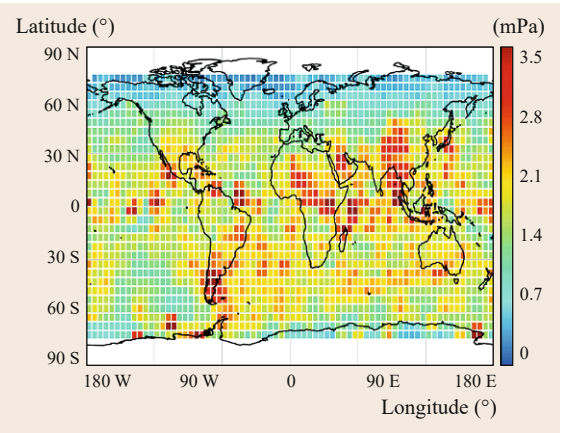

Fig. 38.23 Horizontal momentum flux (MF, a measure for horizontal energy transport by gravity waves) distribution generated from groupings of three co-located GPS RO profiles from the FormoSAT-3/COSMIC mission as 4-year mean values (2007–2010) for July for the altitude range of 20–25 km (courtesy of A. Faber, GFZ)

(PBL) inversions to the overall climate system. The PBL is the lowermost atmospheric layer directly affected by the Earth's surface. Commonly, the boundary between this turbulently mixed layer and the stably stratified atmosphere above is characterized by a temperature inversion and the decrease of relative and absolute humidity, especially in the moist tropics and subtropics. The top of the PBL is sharper and horizontally more homogeneous in the subtropics, where it is often called a trade wind inversion, than in the tropics and over oceans compared to land. The depth of the PBL is an important parameter for numerical weather prediction and climate models. The key property of GNSS RO for monitoring the PBL is global coverage and high vertical resolution; especially, the top of the PBL is associated with sharp vertical refractivity gradients, which can be clearly identified with GNSS RO (Fig. 38.24).

Several studies from different research groups were performed in recent years [38.94, 113, 114]. For example, in [38.113], three-year climatologies of mean PBL heights, derived from GNSS RO (Fig. 38.24) and ECMWF Reanalysis Interim (ERA-Int), show similar spatial and seasonal variations, but the GNSS RO heights were higher by 500 m, and the standard deviation was also higher from GNSS RO, especially in the tropics, which was analyzed in more detail for various regions, as the Pacific Ocean and the Sahara desert. The results suggest that the underlying causes of the bias between GNSS RO and ERA-Int likely vary from region to region. Another main result of this study is the statement that GNSS RO profiles actually contain vertically resolved information above and within the PBL, information which can be difficult to obtain through any other satellite measurement.

38.2.9 Synergy of GNSS Radio Occultation with Reflectometry

Recently, GNSS signals reflected off the surface of the Earth are in focus of intense international GNSS research (GNSS-Reflectometry, GNSS-R). These signals promise a broad range and numerous geophysical applications for remote sensing (e.g., [38.115, 116]) and are in more detail focused in Chap. 40 of this book. Whereas GNSS atmosphere sounding is already fully recognized as an established atmospheric remote-sensing technique, GNSS-R needs more and concentrated international research to exploit its full and

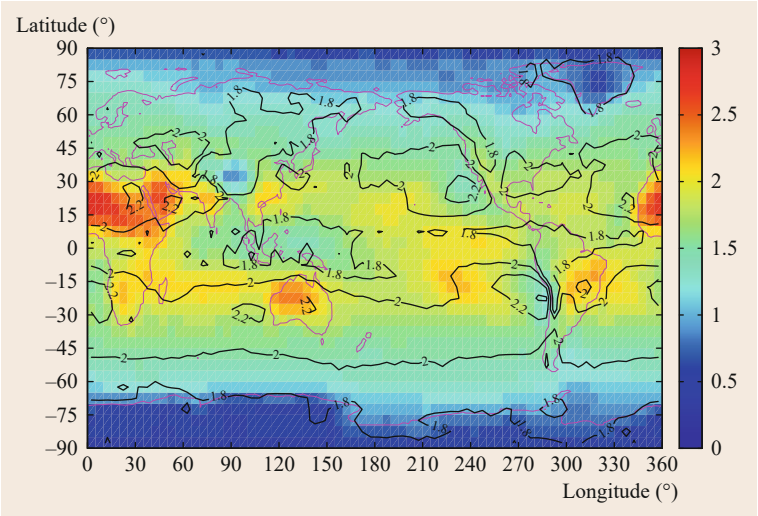

Fig. 38.24 Height of the mean global PBL (resolution $5 \times 5°$, derived from five years of GPS RO data from the FormoSAT-3/COSMIC mission (2007–2011) (courtesy of C.O. Ao, JPL)

unique potential for the remote sensing of water, ice, and land surfaces but also for atmosphere/ionosphere sounding. Important milestones for this development are the dedicated satellite missions CYGNSS (CYclone Global Navigation Satellite System, National Aeronautics and Space Administration (NASA), [38.117]) and GEROS-ISS (GNSS Reflectometry Radio Occultation and Scatterometry aboard the International Space Station; European Space Agency (ESA) [38.115]), which focus on a global application of the GNSS reflectometry.

Part of these activities is the investigation of the potential of the carrier-phase interferometry between the reflected and direct occultation signals (coherent reflectometry), which was initially demonstrated using the measurements from GPS/MET and CHAMP [38.118–120], see Fig. 38.25. These studies indicated that submeter sensitivity on the surface heights can formally be reached with this technique, which offers potential altimetric applications of ocean and ice surfaces. Improved and specific GNSS-tracking software probably can improve this reached accuracy in future with combined occultation/reflection experiments. A major advantage of the coherent reflectometry compared to nadir-viewing reflectometry is that only a low-gain limb-viewing antenna is required, which allows the application also aboard small satellites in future GNSS remote-sensing constellations. But for such application, a more detailed evaluation of the accuracy potential of the coherent reflectometry is required.

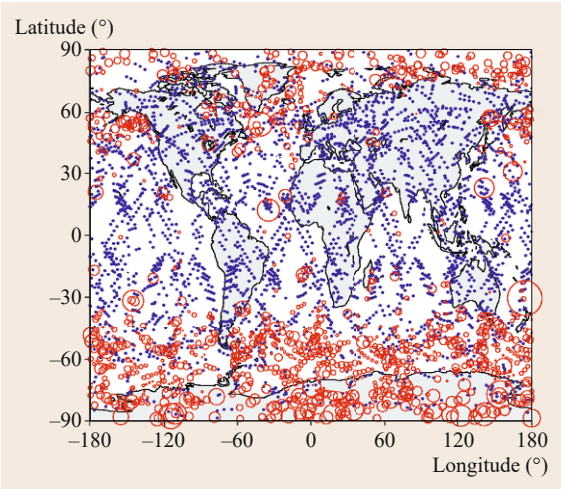

Fig. 38.25 Geographical distribution of 3783 occultation events observed between 14 May and 10 June 2001. *Blue dots* indicate 2571 observations without reflection signatures; 1212 reflection events are marked as *red circles*. Circle diameter is proportional to the reflected intensity (courtesy of G. Beyerle, GFZ)

38.3 Outlook

Ground- and satellite-based atmosphere sounding techniques with their broad spectrum of applications, especially in weather forecast and climate change-related research, were introduced. An overview of the main applications is presented in Table 38.2. Today many thousands of continuously operating ground-based stations exist. Some hundreds are coordinated globally by the IGS and many more are coordinated on a regional or local (national) level. For real-time applications such as weather forecasting, the most important information is the temporal variations, the timing of moving air masses. This does not necessarily require an absolute calibration and homogeneous processing. In this aspect, the monitoring of the water vapor content over decades, for climate change studies, is much more demanding in terms of homogeneous networks and processing in order to draw correct conclusions for the very tiny trends that are expected.

The ground-based data have so far mainly been acquired from sites on land. Platforms on ships or bouys, have more logistics involved and suffer of some extent from the need for simultaneous estimates of the vertical coordinate. The concept has been demonstrated (see [38.121, 122]) and assuming more efficient data communication in the future this may offer a much improved global coverage.

Beginning with the initial and very successful measurements from GPS/MET and by the follow-on missions, as, for example, CHAMP, GRACE, FormoSAT-3/COSMIC and Metop, the innovative GNSS RO method became an established atmospheric remote-sensing technique within the last two decades. A series of new missions is planned and will be realized within the coming years. Our general conclusion is that GNSS atmosphere sounding, ground as well as satellite based, underwent a revolutionary development especially during the last decade and are now fully recognized atmospheric remote-sensing techniques. This development is documented by a broad variety of scientific and also operational applications, most visible is the continuous use of ground- and satellite-based GNSS data for the improvement of numerical weather forecasts since 2006.

The recent GNSS developments will further push these activities. There are upcoming and modernized transmitter systems, continuously increasing receiver

Table 38.2 GNSS meteorology applications for remote sensing of the neutral atmosphere

Application	Ground-based receivers	Satellite-based receivers
Weather forecasting		
IWV timeseries	Yes	–
Bending angle/Refractivity profiles	–	Yes
Climate		
IWV trends	Yes	–
Annual and diurnal IWV signals	Yes	–
Global Temperature trends	–	Yes
Tropopause characteristics	–	Yes
Atmospheric research		
Atmospheric convection regional scale	Yes	–
Atmospheric waves	–	Yes
Complement other sensors (e.g., infrared)	–	Yes
Large scale atmospheric circulation	–	Yes
Planetary boundary layer	–	Yes
Tropical cyclones	–	Yes
Upper troposphere and lower stratosphere	–	Yes
3D-Distributions of water vapor	Yes	–
Spatiotemporal variability in the IWV	Yes	–

infrastructure, with the extension of ground networks and more GNSS flight receivers, but probably also new marine, ground and flight platforms in the near future, not to forget the *everyones* receivers such as smartphones.

These developments will not only increase the number of atmospheric GNSS measurements, but probably also will allow a better data quality. It will further stimulate the existing applications but probably also will open the door for new and innovative applications. GNSS atmosphere sounding is a story of success, which will be continuously updated.

Acknowledgments. The authors want to thank several colleagues for providing information and figures: Chi On Ao (JPL), Christina Arras (GFZ), Georg Beyerle (GFZ), Galina Dick (GFZ), Axel von Engeln (EUMETSAT), Antonia Faber (GFZ), Rüdiger Haas (Chalmers), Sean Healy (ECMWF), Stefan Heise (GFZ), Tong Ning (Swedish Mapping, Cadastral and Land Registration Authority), Torsten Schmidt (GFZ), Hans-Georg Scherneck (Chalmers), Bill Schreiner (UCAR), Andrea Steiner (Wegener Center), Tom Yunck (GeoOptics), and Florian Zus (GFZ).

References

38.1 D.M. Tralli, T.H. Dixon, S.A. Stephens: Effect of wet tropospheric path delays on estimation of geodetic baselines in the Gulf of California using the Global Positioning System, J. Geophys. Res. **93**(B6), 6545–6557 (1988)

38.2 D.M. Tralli, S.M. Lichten: Stochastic estimation of tropospheric path delays in Global Positioning System geodetic measurements, Bull. Geod. **64**, 127–159 (1990)

38.3 Y.E. Bar-Sever, P.M. Kroger, A.J. Börjesson: Estimating horizontal gradients of tropospheric path delay with a single GPS receiver, J. Geophys. Res. **103**, 5019–5035 (1998)

38.4 P. Elosegui, J.L. Davis: Accuracy assessment of GPS slant-path determinations, Int. Workshop GPS Meteorol., Tsukuba, ed. by T. Iwabuchi, Y. Shoji (Meteorological Society of Japan, Tsukuba 2004) pp. 1–6

38.5 A.E. Niell: Global mapping functions for the atmosphere delay at radio wavelengths, J. Geophys. Res. **101**(B2), 3227–3246 (1996)

38.6 I.D. Thomas, M.A. King, P.J. Clarke, N.T. Penna: Precipitable water vapor estimates from homogeneously reprocessed GPS data: An intertechnique comparison in Antarctica, J. Geophys. Res. **116**, D19101 (2011)

38.7 T.A. Herring: Precision of vertical position estimates from very long baseline interferometry, J. Geophys. Res. **91**, 9177–9182 (1986)

38.8 S. Kedar, G.A. Hajj, B.D. Wilson, M.B. Heflin: The effect of the second order GPS ionospheric correction on receiver positions, Geophys. Res. Lett. **30**(16), 1829 (2003)

38.9 M. Hernandez-Pajares, J.M. Juan, J. Sanz, R. Ors: Second-order ionospheric term in GPS: Implementation and impact on geodetic estimates, J. Geophys. Res. **112**, B08417 (2007)

38.10 E.J. Petrie, M.A. King, P. Moore, D.A. Lavallè: Higher-order ionospheric effects on the GPS reference frame and velocities, J. Geophys. Res. **115**(10), B03417 (2013)

38.11 R. Schmid, P. Steigenberger, G. Gendt, M. Ge, M. Rothacher: Generation of a consistent absolute phase center correction model for GPS receiver and satellite antennas, J. Geod. **81**(5), 781–798 (2007)

38.12 P.O. Jarlemark, T.R. Emardson, J.M. Johansson, G. Elgered: Ground-based GPS for validation of climate models: The impact of satellite antenna phase center variations, IEEE Trans. Geosci. Remote Sens. **GE-48**(10), 3847–3854 (2010)

38.13 T. Ning, G. Elgered, J.M. Johansson: The impact of microwave absorber and radome geometries on GNSS measurements of station coordinates and atmospheric water vapour, Adv. Space Res. **47**, 186–196 (2011)

38.14 National Institute of Standards and Technology, US, http://physics.nist.gov/cgi-bin/cuu/Value?r

38.15 J.L. Davis, T.A. Herring, I.I. Shapiro, A.E.E. Rogers, G. Elgered: Geodesy by radio interferometry: Effects of atmospheric modeling errors on estimates of baseline length, Radio Sci. **20**(6), 1593–1607 (1985)

38.16 S. Heise, G. Dick, G. Gendt, T. Schmidt, J. Wickert: Integrated water vapor from IGS ground-based GPS observations: Initial results from a 5-min data set, Ann. Geophysicae **27**, 2851–2859 (2009)

38.17 T. Nilsson, G. Elgered: Long-term trends in the atmospheric water vapor content estimated from ground-based GPS data, J. Geophys. Res. **113**(D19101), 1–12 (2008)

38.18 S. Vey, R. Dietrich, M. Fritsche, A. Rülke, P. Steigenberger, M. Rothacher: On the homogeneity and interpretation of precipitable water time series derived from global GPS observations, J. Geophys. Res. **114**(D10101), 1–15 (2009)

38.19 K. Lagler, M. Schindelegger, J. Böhm, H. Krásná, T. Nilsson: GPT2: Empirical slant delay model for radio space geodetic techniques, Geophys. Res. Lett. **40**, 1069–1073 (2013)

38.20 R.B. Stull: *An introduction +to boundary layer meteorology*, 3rd edn. (Academic Press, San Diego 1992)

38.21 J.P. Hauser: Effects of deviations from hydrostatic equilibrium on atmospheric corrections to satellite and lunar laser range measurements, J. Geophys. Res. **94**, 10182–10186 (1991)

38.22 M. Bevis, S. Chiswell, T.A. Herring, R.A. Anthes, C. Rocken, R.H. Ware: GPS meteorology: Mapping zenith wet delays onto precipitable water, J. Appl. Meteorol. **33**, 379–386 (1994)

38.23 J. Wang, L. Zhang, A. Dai: Global estimates of water-vapor-weighted mean temperature of the atmosphere for GPS applications, J. Geophys. Res. **110**(D21101), 1–17 (2005)

38.24 T.R. Emardson, G. Elgered, J.M. Johansson: Three Months of continuous monitoring of atmospheric water vapor with a network of Global Positioning System receivers, J. Geophys. Res. **103**, 1807–1820 (1998)

38.25 T.R. Emardson, H.J.P. Derks: On the Relation Between the Wet Delay and the Integrated Precipitable Water Vapour in the European Atmosphere, Meteorol. Appl. **7**, 61–68 (2000)

38.26 G.S. Kell: Density, thermal expansivity, and compressibility of liquid water from 0 to 150 °C: Correlations and tables for atmospheric pressure and saturation reviewed and expressed on 1968 temperature scale, J. Chem. Engineering Data **20**(1), 97–105 (1975)

38.27 G. Elgered, J.M. Johansson, B.O. Rönnäng, J.L. Davis: Measuring regional atmospheric water vapor using the Swedish permanent GPS network, Geophys. Res. Lett. **24**, 2663–2666 (1997)

38.28 J.L. Davis, G. Elgered: The spatio-temporal structure of GPS water-vapor determinations, Phys. Chem. Earth **23**(1), 91–96 (1998)

38.29 T.R. Emardson, F.H. Webb: Estimating the motion of atmospheric water vapor using the Global Positioning System, GPS Solutions **6**, 58–64 (2002)

38.30 EUMETNET, The Network of European Meteorological Services, http://egvap.dmi.dk/

38.31 H.-S. Bauer, V. Wulfmeyer, T. Schwitalla, F. Zus, M. Grzeschik: Operational assimilation of GPS slant path delay measurements into the MM5 4DVAR system, Tellus **63A**, 263–282 (2011)

38.32 P. Poli, P. Moll, F. Rabier, G. Desroziers, B. Chapnik, L. Berre, S.B. Healy, E. Andersson, F.-Z. El Guelai: Forecast impact studies of zenith total delay data from European near real-time GPS stations in Météo France 4DVAR, J. Geophys. Res. **112**(D06114), 1–16 (2007)

38.33 M. Bender, G. Dick, M. Ge, Z. Deng, J. Wickert, H.-G. Kahle, A. Raabe, G. Tetzlaff: Operational assimilation of GPS zenith total delay observations into the Met Office numerical weather prediction models, Mon. Weather Rev. **140**, 2706–2719 (2012)

38.34 R. Eresmaa, H. Järvinen: An observation operator for ground-based GPS slant delays, Tellus **58A**, 131–140 (2006)

38.35 T. Nilsson, L. Gradinarsky: Water vapor tomography using GPS phase observations: Simulation results, IEEE Trans. Geosci. Remote Sens. **GE-44**(10), 2927–2941 (2006)

38.36 M. Bender, G. Dick, M. Ge, Z. Deng, J. Wickert, H.-G. Kahle, A. Raabe, G. Tetzlaff: Development of a GNSS water vapour tomography system using algebraic reconstruction techniques, Adv. Space Res. **47/10**, 1704–1720 (2011)

38.37 A. Flores, G. Ruffini, A. Rius: 4D tropospheric tomography using GPS slant wet delays, Annal. Geophysicae **18**, 223–234 (2001)

38.38 S.A. Buehler, A. von Engeln, E. Brocard, V.O. John, T. Kuhn, P. Eriksson: Recent developments in the line-by-line modeling of outgoing longwave radiation, J. Quant. Spectrosc. Radiat. Transfer **98**(3), 446–457 (2006)

38.39 N.D. Gordon, A.K. Jonko, P.M. Forster, K.M. Shell: An observationally based constraint on the water-vapor feedback, J. Geophys. Res. **118**, 12435–12443 (2014)

38.40 D.J. Seidel, F.H. Berger, H.J. Diamond, J. Dykema, D. Goodrich, F. Immler, W. Murray, T. Peterson, D. Sisterson, M. Sommer, P. Thorne, H. Vömel, J. Wang: Reference upper-air observations for climate: Rationale, progress, and plans, Bull. Am. Meteorol. Soc. **90**, 361–369 (2009)

38.41 H.-G. Scherneck, J.M. Johansson, H. Koivula, T. van Dam, J.L. Davis: Vertical crustal motion observed in the BIFROST project, J. Geodyn. **35**, 425–441 (2003)

38.42 T. Ning, G. Elgered: Trends in the atmospheric water vapor content from ground-based GPS: The impact of the elevation cutoff angle, IEEE J-STARS **5**(3), 744–751 (2012)

38.43 S. Jin, O.F. Luo: Variability and Climatology of PWV From Global 13-Year GPS Observations, IEEE Trans. Geosci. Remote Sens. **GE-47**, 1918–1924 (2009)

38.44 J.P. Ortiz de Galisteo, Y. Bennouna, C. Toledano, V. Cachorro, P. Romero, M.I. Andrès, B. Torres: Analysis of the annual cycle of the precipitable water vapour over Spain from 10-year homogenized series of GPS data, Quart. J. Roy. Meteorol. Soc. **139**, 948–958 (2013)

38.45 Y.S. Bennouna, B. Torres, V.E. Cachorro, J.P. Ortiz de Galisteo, C. Toledano: The evaluation of the integrated water vapour annual cycle over the Iberian Peninsula from EOS-MODIS against different ground-based techniques, Quart. J. Roy. Meteorol. Soc. **139**, 1935–1956 (2013)

38.46 S. Jin, O.F. Luo, S. Gleason: Characterization of diurnal cycles in ZTD from a decade of global GPS observations, J. Geod. **83**, 537–545 (2009)

38.47 J. Wang, L. Zhang: Climate applications of a global, 2-hourly atmospheric precipitable water dataset derived from IGS tropospheric products, J. Geod. **83**, 209–217 (2009)

38.48 S. Pramualsakdikul, R. Haas, G. Elgered, H.-G. Scherneck: Sensing of diurnal and semi-diurnal variability in the water vapour content in the tropics using GPS measurements, Meteorol. Appl. **14**, 403–412 (2007)

38.49 E. Jakobson, H. Ovril, G. Elgered: Diurnal variability of precipitable water in the Baltic region, impact on transmittance of the direct solar radiation, Boreal Environment Res. **14**, 45–55 (2009)

38.50 S. Vey, R. Dietrich, A. Rülke, M. Fritsche, P. Steigenberger, M. Rothacher: Validation of precipitable water vapor within the NCEP/DOE reanalysis using global GPS observations from one decade, J. Climate **23**, 1675–1695 (2010)

38.51 T. Ning, G. Elgered, U. Willén, J.M. Johansson: Evaluation of the atmospheric water vapor content in a regional climate model using ground-based GPS measurements, J. Geophys. Res. **118**, 329–339 (2013)

38.52 C. Rocken, R. Anthes, M. Exner, D. Hunt, S. Sokolovskiy, R. Ware, M. Gorbunov, W. Schreiner, D. Feng, B. Herman, Y.-H. Kuo, X. Zou: Analysis and validation of GPS/MET data in the neutral atmosphere, J. Geophys. Res. **102**, 29849–29866 (1997)

38.53 R. Ware, D. Exner, M. Feng, M. Gorbunov, K. Hardy, B. Herman, Y. Kuo, T.K. Meehan, W.G. Melbourne, C. Rocken, W. Schreiner, S. Sokolovskiy, F. Solheim, X. Zou, R. Anthes, S. Businger, K. Trenberth: GPS sounding of the atmosphere from low Earth orbit – Preliminary results, Bull. Am. Met. Soc. **77**, 19–40 (1996)

38.54 E.R. Kursinski, G.A. Hajj, K.R. Hardy, J.T. Schofield, R. Linfield: Observing the Earth's atmosphere with radio occultation measurements using the Global Positioning System, J. Geophys. Res. **102**, 23429–23465 (1997)

38.55 R.A. Anthes, P.A. Bernhardt, Y. Chen, K. Cucurull, K.F. Dymond, S. Ector, S.B. Healy, S.-P. Ho, D.C. Hunt, Y.-H. Kuo, H. Liu, K. Manning, C. McCormick, T.K. Meehan, W.J. Randel, C. Rocken, W.S. Schreiner, S.V. Sokolovskiy, S. Syndergaard, D.C. Thompson, K.E. Trenberth, T.-K. Wee, N.L. Yen, Z. Zhang: The COSMIC/Formosat-3 Mission: Early results, Bull. Am. Met. Soc. **89**(3), 313–333 (2008)

38.56 S. Healy: Operational assimilation of GPS radio occultation measurements at ECMWF, ECMWF Newsletter 111 (2007)

38.57 J. Wickert, C. Reigber, G. Beyerle, R. König, C. Marquardt, T. Schmidt, L. Grunwaldt, R. Galas, T.K. Meehan, W.G. Melbourne, K. Hocke: Atmosphere sounding by GPS radio occultation: First results from CHAMP, Geophys. Res. Lett. **28**(17), 3263–3266 (2001)

38.58 J. Wickert, R. Galas, G. Beyerle, R. König, C. Reigber: GPS ground station data for CHAMP radio occultation measurements, PCE **26**(6–8), 503–511 (2001)

38.59 G.A. Hajj, E.R. Kursinski, L.J. Romans, W.I. Bertiger, S.S. Leroy: A technical description of atmospheric sounding by GPS occultation, J. Atmos. Sol.-Terr. Phys. **64**, 451–469 (2002)

38.60 W.G. Melbourne, E. Davis, C. Duncan, G. A. Hajj, K. Hardy, E. Kursinski, T. Meehan, L. Young: The application of spaceborne GPS to atmospheric limb sounding and global change monitoring Publication 94-18 (Jet Propulsion Laboratory, Pasadena 1994)

38.61 J. Wickert, G. Beyerle, G.A. Hajj, V. Schwieger, C. Reigber: GPS radio occultation with CHAMP: Atmospheric profiling utilizing the space-based single difference technique, Geophys. Res. Lett. **29**(81187), 1–4 (2002)

38.62 G. Beyerle, T. Schmidt, G. Michalak, S. Heise, J. Wickert, C. Reigber: GPS radio occultation with GRACE: Atmospheric profiling utilizing the zero difference technique, Geophys. Res. Lett. **32**(L13806), 1–5 (2005)

38.63 M.E. Gorbunov, S.V. Sokolovskiy, L. Bengtsson: Space refractive tomography of the atmosphere: Modeling of direct and inverse problems, Report 210 (Max Planck Institute for Meteorology, Hamburg 1996)

38.64 V.V. Vorob'ev, T.G. Krasil'nikova: Estimation of the accuracy of the atmospheric refractive index recovery from doppler shift measurements at

frequencies used in the NAVSTAR system, Phys. Atmos. Ocean **29**, 602–609 (1994)
38.65 E.K. Smith, S. Weintraub: The constants in the equation for atmospheric refractive index at radio frequencies, Proc. IRE **41**, 1035–1037 (1953)
38.66 K. Hocke: Inversion of GPS meteorology data, Annales Geophysicae **15**, 443–450 (1997)
38.67 M.E. Gorbunov, S.V. Sokolovskiy: Remote sensing of refractivity from space for global observations of atmospheric parameters, Report 119 (Max Planck Institute for Meteorology, Hamburg 1993)
38.68 C. Marquardt, K. Labitzke, Ch. Reigber, T. Schmidt, J. Wickert: An assessment of the quality of GPS/MET radio limb soundings during February 1997, Phys. Chem. Earth **26**, 125–130 (2001)
38.69 S. Heise, J. Wickert, G. Beyerle, T. Schmidt, C. Reigber: Global monitoring of tropospheric water vapor with GPS radio occultation aboard CHAMP, Adv. Space Res. **27**, 2222–2227 (2006)
38.70 S. Healy, J. Eyre: Retrieving temperature, water vapor and surface pressure information from refractive-index profiles derived by radio occultation: A simulation study, Quart. J. Roy. Meteorol. Soc. **126**, 1661–1683 (2000)
38.71 M.A. Ringer, S.B. Healy: Monitoring twenty-first century climate using GPS radio occultation bending angles, Geophys. Res. Lett. **35**(L05708), 1–6 (2007)
38.72 G. Beyerle, T. Schmidt, J. Wickert, S. Heise, M. Rothacher, G. König-Langlo, K.B. Lauritsen: Observations and simulations of receiver-induced refractivity biases in GPS radio occultation, J. Geophys. Res. **111**(D12101), 1–13 (2006)
38.73 S.V. Sokolovskiy, C. Rocken, D. Hunt, W. Schreiner, J. Johnson, D. Masters, S. Esterhuizen: GPS profiling of the lower troposphere from space: Inversion and demodulation of the open-loop radio occultation signals, Geophys. Res. Lett. **33**(L14816), 1–5 (2006)
38.74 C.O. Ao, T.K. Meehan, G.A. Hajj, A.J. Mannucci, G. Beyerle: Lower-troposphere refractivity bias in GPS occultation retrievals, J. Geophys. Res. **108**(D18), 4577 (2003)
38.75 A.S. Jensen, M. Lohmann, H.H. Benzon, A. Nielsen: Full spectrum in version of radio occultation signal, Radio Sci. **38**(3), 1–15 (2003)
38.76 M.E. Gorbunov: Canonical transform method for processing radio occultation data in the lower troposphere, Radio Sci. **37**(5), 1076 (2002)
38.77 C.O. Ao, A.J. Mannucci, E.R. Kursinski: Improving GPS radio occultation stratospheric refractivity for climate benchmarking, Geophys. Res. Lett. **39**(L12701), 1–6 (2012)
38.78 A.J. Mannucci, C.O. Ao, L.E. Young, T.K. Meehan: Studying the atmosphere using global navigation satellites, EOS Trans. **95**(43), 389–390 (2014)
38.79 J. Wickert, G. Michalak, T. Schmidt, G. Beyerle, C.Z. Cheng, S.B. Healy, S. Heise, C.Y. Huang, N. Jakowski, W. Köhler, C. Mayer, D. Offiler, E. Ozawa, A.G. Pavelyev, M. Rothacher, B. Tapley, C. Arras: GPS radio occulation: Results from CHAMP, GRACE and FORMOSAT-3/COSMIC, Terr. Atmos. Ocean. Sci. **1**, 35–50 (2009)
38.80 S.B. Healy, J. Wickert, G. Michalak, T. Schmidt, G. Beyerle: Combined forecast impact of GRACE-A and CHAMP GPS radio occultation bending angle profiles, Atmos. Sci. Lett. **8**, 43–50 (2007)
38.81 S. Healy, A. Jupp, C. Marquardt: Forecast impact experiment with GPS radio occultation measurements, Geophys. Res. Lett. **32**(L03804), 1–4 (2005)
38.82 A.K. Steiner, B.C. Lackner, F. Ladstädter, B. Scherllin-Pirscher, U. Foelsche, G. Kirchengast: GPS radio occultation for climate applications, Radio Sci. **46**(RS0D24), 1–17 (2011)
38.83 T. Schmidt, J. Wickert, A. Haser: Variability of the upper troposphere and lower stratosphere observed with GPS radio occultation temperature-sariability of the upper troposphere and lower stratosphere observed with GPS radio occultation bending angles and temperatures, Adv. Space Res. **46**(2), 150–161 (2010)
38.84 T. Schmidt, J. Wickert, G. Beyerle, S. Heise: Global tropopause height trends estimated from GPS radio occultation data, Geophys. Res. Lett. **35**(L11806), 1–5 (2008)
38.85 A.K. Steiner, D. Hunt, S.P. Ho, G. Kirchengast, A.J. Mannucci, B. Scherllin-Pirscher, H. Gleisner, A. von Engeln, T. Schmidt, C. Ao, S.S. Leroy, E.R. Kursinski, U. Foelsche, M. Gorbunov, S. Heise, Y.H. Kuo, K.B. Lauritsen, C. Marquardt, C. Rocken, W. Schreiner, S. Sokolovskiy, S. Syndergaard, J. Wickert: Quantification of structural uncertainty in climate data records from GPS radio occultation, Atmos. Chem. Phys. **13**, 1469–1484 (2013)
38.86 S.P. Ho, D. Hunt, A.K. Steiner, A.J. Mannucci, G. Kirchengast, H. Gleisner, S. Heise, A. von Engeln, C. Marquardt, S. Sokolovskiy, W. Schreiner, B. Scherllin-Pirscher, C.O. Ao, J. Wickert, S. Syndergaard, K.B. Lauritsen, S. Leroy, E.R. Kursinski, Y.H. Kuo, U. Foelsche, T. Schmidt, M. Gorbunov: Reproducibility of GPS radio occultation data for climate monitoring: Profile-to-profile inter-comparison of CHAMP climate records 2002 to 2008 from six data centers, J. Geophys. Res. **117**, D18111 (2012)
38.87 S.P. Ho, G. Kirchengast, S. Leroy, J. Wickert, A. Mannucci, A. Steiner, C.O. Ao, M. Borsche, A. von Engeln, U. Foelsche, S. Heise, D. Hunt, B. Iijima, Y.H. Kuo, R. Kursinski, B. Lackner, B. Pirscher, M. Ringer, C. Rocken, T. Schmidt, W. Schreiner, S. Sokolovskiy: Estimating the uncertainty of using GPS radio occultation data for climate monitoring: Intercomparison of CHAMP refractivity climate records from 2002 to 2006 from different data centers, J. Geophys. Res. **114**, D23107 (2009)
38.88 A. von Engeln, S. Healy, C. Marquardt, Y. Andres, F. Sancho: Validation of operational GRAS radio occultation data, Geophys. Res. Lett. **36**(L1780), 1–4 (2009)
38.89 F. Zus, G. Beyerle, L. Grunwaldt, S. Heise, G. Michalak, T. Schmidt, J. Wickert: Atmosphere sounding by GPS radio occultation: First results from TanDEM-X and comparison with TerraSAR-X,

Adv. Space Res. **53**(2), 272–279 (2014)
38.90 Status of the Global Observing System for Radio Occultation (Update 2013), IROWG/DOC/2013/02 (IROWG, 2013). http://www.irowg.org
38.91 Y.-H. Kuo, W.S. Schreiner, J. Wang, D.L. Rossiter, Y. Zhang: Comparison of GPS radio occultation soundings with radiosondes, Geophys. Res. Lett. **32**, 1–4 (2005)
38.92 W. Schreiner, C. Rocken, S. Sokolovskiy, S. Syndergaard, D. Hunt: Estimates of the precision of GPS radio occultations from the COSMIC/Formosat-3 mission, Geophys. Res. Lett. **34**(L04808), 1–5 (2007)
38.93 G.F. Lindal, G.E. Wood, H.B. Hotz, D.N. Sweetnam, V.R. Eshleman, G.L. Tyler: The atmosphere of Titan: An analysis of the Voyager 1 radio occultation measurements, Icarus **53**, 348–363 (1983)
38.94 Y.-H. Sokolovskiy, S.V. Kuo, C. Rocken, W.S. Schreiner, D. Hunt, R.A. Anthes: Monitoring the atmospheric boundary layer by GPS radio occultation signals recorded in the open-loop mode, Geophys. Res. Lett. **33**, L12813 (2006)
38.95 S.P. Ho, M. Goldberg, Y.-H. Kuo, Z.Z. Zou, W. Schreiner: Calibration of temperature in the lower stratosphere from microwave measurements using COSMIC radio occultation data: Preliminary results, Terr. Atmos. Ocean. Sci. **20**(1), 87–100 (2009)
38.96 J. Wickert, C. Arras, G. Beyerle, M. Ge, F. Flechtner, S.B. Healy, S. Heise, C.Y. Huang, B. Kuo, C. Marquardt, G. Michalak, N. Jakowski, T. Schmidt, M. Semmling: Radio occultation with navigation satellites: Recent results and prospects with Galileo, Proc. 3rd Int. Coll. Sci. Aspects of Galileo, Copenhagen (ESA, Noordwijk 2011)
38.97 L. Cucurull: Improvement in the use of an operational constellation of GPS radio occultation receivers in weather forecasting, Wea. Forecast. **25**, 749–767 (2010)
38.98 J. Aparicio, G. Deblonde: Impact of the assimilation of CHAMP refractivity profiles in Environment Canada global forecasts, Mon. Weather Rev. **136**, 257–275 (2008)
38.99 P. Poli, S. Healy, F. Rabier, J. Pailleux: Preliminary assessment of the scalability of GPS radio occultations impact in numerical weather prediction, Geophys. Res. Lett. **35**(L23811), 1–5 (2008)
38.100 F. Harnisch, S.B. Healy, P. Bauer, J. Engish: Scaling of GNSS radio occultation impact with observation number using an ensemble of data assimilations, Mon. Weather Rev. **149**, 4395–4413 (2013)
38.101 B. Scherllin-Pirscher, C. Deser, S.P. Ho, C. Chou, W. Randel, Y.-H. Kuo: The vertical and spatial structure of ENSO in the upper troposphere and lower stratosphere from GPS radio occultation measurements, Geophys. Res. Lett. **39**(L20801), 1–6 (2012)
38.102 A.J. Mannucci, C.O. Ao, T.P. Yunck, L.E. Young, G.A. Hajj, B.A. Iijima, D. Kuang, T.K. Meehan, S.S. Leroy: Generating climate benchmark atmospheric soundings using GPS occultation data. In: *Atmospheric and Environmental Remote Sensing Data Processing and Utilization II: Perspective on Calibration/Validation Initiatives and Strategies*, ed. by H.L. Huang, H.J. Bloom (International Society for Optical Engineering, Bellingham, WA, 630108 2006) p. 630108
38.103 B.C. Lackner, A.K. Steiner, G.C. Hegerl, G. Kirchengast: Atmospheric climate change detection by radio occultation data using a fingerprinting method, J. Climate **24**, 5275–5291 (2011)
38.104 B.C. Santer, T.M.L. Wigley, A.J. Simmons, P.W. Kållberg, G.A. Kelly, S.M. Uppala, C. Ammann, J.S. Boyle, W. Brüggemann, C. Doutriaux, M. Fiorino, C. Mears, G.A. Meehl, R. Sausen, K.E. Taylor, W.M. Washington, M.F. Wehner, F.J. Wentz: Identification of anthropogenic climate change using a second-generation reanalysis, J. Geophys. Res. **109**, D21104 (2004)
38.105 R. Sausen, B.D. Santer: Use of changes in tropopause height to detect human influences on climate, Meteorologische Zeitschrift **12**, 131–136 (2003)
38.106 T. Schmidt, G. Beyerle, S. Heise, J. Wickert, M. Rothacher: A climatology of multiple tropopauses derived from GPS radio occultations with CHAMP and SAC-C, Geophys. Res. Lett. **33**(L04808), 1–4 (2006)
38.107 W.J. Randel, F. Wu, W.R. Rios: Thermal variability of the tropical tropopause region derived from GPS/MET observations, J. Geophys. Res. **108**(D1, 4024), 1–12 (2003)
38.108 M. Nishida, A. Shimizu, T. Tsuda, C. Rocken, R.H. Ware: Seasonal and longitudinal variations in the tropical tropopause observed with the GPS occultation technique (GPS/MET), J. Meteorol. Soc. Jpn. **78**, 691–700 (2000)
38.109 T. Schmidt, J. Wickert, G. Beyerle, S. Heise: Global tropopause height trends estimated from GPS radio occultation data, Geophys. Res. Lett. **35**, L11806 (2008)
38.110 T. Tsuda, M. Nishida, C. Rocken, R.H. Ware: A global morphology of gravity wave activity in the stratosphere revealed by the GPS occultation data (GPS/MET), J. Geophys. Res. **105**, 7257–7273 (2000)
38.111 A. Faber, P. Llamedo, T. Schmidt, A. de la Torre, J. Wickert: On the determination of gravity wave momentum flux from GPS radio occultation data, Atmos. Meas. Tech. **6**, 3169–3180 (2013)
38.112 C. Arras, J. Wickert, C. Jacobi, G. Beyerle, S. Heise, T. Schmidt: Global sporadic E characteristics obtained from GPS radio occultation measurements. In: *Climate And Weather of the Sun-Earth System (CAWSES): Highlights from a priority program*, ed. by F.-J. Luebken (Springer, Berlin 2013) pp. 207–221
38.113 C.O. Ao, D.E. Waliser, S.K. Chan, J.L. Li, B. Tian, F. Xie, A.J. Mannucci: Planetary boundary layer heights from GPS radio occultation refractivity and humidity profiles, J. Geophys. Res. **117**(D16117), 1–18 (2012)
38.114 A. von Engeln, J. Teixeira, J. Wickert, S.A. Buehler: Using CHAMP radio occultation data to determine the top altitude of the Planetary Boundary Layer, Geophys. Res. Lett. **32**(L06815), 1–4 (2005)

38.115 J. Wickert, E. Cardellach, M. Martin-Neira, J. Bandeiras, L. Bertino, O.B. Andersen, A. Camps, N. Catarino, B. Chapron, F. Fabra, N. Floury, G. Foti, C. Gommenginger, J. Hatton, P. Høeg, A. Jäggi, M. Kern, T. Lee, Z. Li, H. Park, N. Pierdicca, G. Ressler, A. Rius, J. Rosello, J. Saynisch, N. Soulat, C.K. Shum, M. Semmling, A. Sousa, J. Xie, C. Zuffada: GEROS-ISS: GNSS REflectometry, Radio Occultation, and Scatterometry Onboard the International Space Station, IEEE J. Sel. Top. Appl. Earth Obs. Remote Sens. **9**(10), 1–30 (2016), doi:10.1109/JSTARS.2016.2614428

38.116 E. Cardellach, F. Fabra, O. Nogués-Correig, S. Oliveras, S. Ribó, A. Rius: GNSS-R ground-based and airborne campaigns for ocean, land, ice and snow techniques: Application to the GOLD-RTR datasets, Radio Sci. **46**(RS0C04), 1–16 (2011)

38.117 C. Ruf, S. Gleason, Z. Jelenak, S. Katzberg, A. Ridley, R. Rose, J. Scherrer, V. Zavorotny: The CYGNSS nanosatellite constellation hurricane mission, Proc. 2012 Int. Geosci. Remote Sens. Symp., Munich (IEEE, 2012) pp. 214–216 doi:10.1109/IGARSS.2012.6351600

38.118 E. Cardellach, C.O. Ao, M. de la Torre Juarez, G.A. Hajj: Carrier phase delay altimetry with GPS – Reflection/occultation interferometry from low Earth orbiters, Geophys. Res. Lett. **31**(L10402), 1–4 (2004)

38.119 G. Beyerle, K. Hocke, J. Wickert, T. Schmidt, C. Marquardt, C. Reigber: GPS radio occultations with CHAMP: A radio holographic analysis of GPS signal propagation in the troposphere and surface reflections, J. Geophys. Res. **107**(D24, 4802), 1–14 (2002)

38.120 A.G. Pavelyev, A.V. Volkov, A.I. Zakharov, S.A. Krutikh, A.I. Kucherjavenkov: Bistatic radar as a tool for Earth investigation using small satellites, Acta Astronaut. **39**(9–12), 721–730 (1996)

38.121 C.D. Chadwell, Y. Bock: Direct estimation of absolute precipitable water in oceanic regions by GPS tracking of a coastal buoy, Geophys. Res. Lett. **28**(19), 3701–3704 (2001)

38.122 C. Rocken, J. Johnson, T.V. Hove, T. Iwabuchi: Atmospheric water vapor and geoid measurements in the open ocean with GPS, Geophys. Res. Lett. **32**, L12813 (2005)